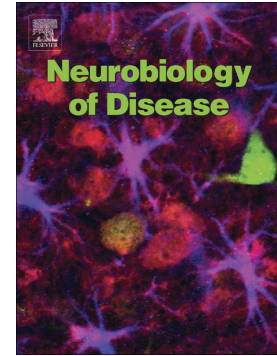


Journal Pre-proof

Doublecortin mutation leads to persistent defects in the Golgi apparatus and mitochondria in adult hippocampal pyramidal cells

M.A. Stouffer, R. Khalaf-Nazzal, C. Cifuentes-Diaz, G. Albertini, E. Bandet, G. Grannec, V. Lavilla, J.-F. Deleuze, R. Olaso, M. Nosten-Bertrand, F. Francis



PII: S0969-9961(22)00094-8

DOI: <https://doi.org/10.1016/j.nbd.2022.105702>

Reference: YNBDI 105702

To appear in: *Neurobiology of Disease*

Received date: 11 October 2021

Revised date: 8 February 2022

Accepted date: 17 March 2022

Please cite this article as: M.A. Stouffer, R. Khalaf-Nazzal, C. Cifuentes-Diaz, et al., Doublecortin mutation leads to persistent defects in the Golgi apparatus and mitochondria in adult hippocampal pyramidal cells, *Neurobiology of Disease* (2022), <https://doi.org/10.1016/j.nbd.2022.105702>

This is a PDF file of an article that has undergone enhancements after acceptance, such as the addition of a cover page and metadata, and formatting for readability, but it is not yet the definitive version of record. This version will undergo additional copyediting, typesetting and review before it is published in its final form, but we are providing this version to give early visibility of the article. Please note that, during the production process, errors may be discovered which could affect the content, and all legal disclaimers that apply to the journal pertain.

Doublecortin mutation leads to persistent defects in the Golgi apparatus and mitochondria in adult hippocampal pyramidal cells

Stouffer MA^{1-3,£}, Khalaf-Nazzal R^{1-3,\$}, Cifuentes-Diaz C¹⁻³, Albertini G¹⁻³, Bandet E^{1-3,#}, Grannec G¹⁻³, Lavilla V⁴, Deleuze J-F⁴, Olasso R⁴, Nosten-Bertrand M¹⁻³, Francis F¹⁻³

¹INSERM UMR-S 1270, Paris 75005, France;

²Sorbonne Université, Université Pierre et Marie Curie, Paris 75005, France;

³Institut du Fer à Moulin, Paris 75005, France

⁴Université Paris-Saclay, CEA, Centre National de Recherche en Génomique Humaine (CNRGH), 91057, Evry, France

£ Current address, Institute of Science and Technology Austria, Klosterneuburg, Austria

\$ Current address, Biomedical Sciences Department, Faculty of Medicine, Arab American University, Jenin P227, Palestine

Current address, Faculty of Medicine, Paris University, Paris

Correspondance to: Fiona Francis, Institut du Fer à Moulin, 17 rue du Fer à Moulin, 75005 Paris France. Email: fiona.francis@inserm.fr

Highlights

- Neurodevelopmental *Dcx* mutation leads to persistent hippocampal abnormalities
- Adult mutant neurons exhibit Golgi apparatus and mitochondria alterations
- In mutant mice, behavioral defects appear earlier and are more severe with aging

Abstract

Human *doublecortin* (*DCX*) mutations are associated with severe brain malformations leading to aberrant neuron positioning (heterotopia), intellectual disability and epilepsy. *DCX* is a microtubule-associated protein which plays a key role during neurodevelopment in neuronal migration and differentiation. *Dcx* knockout (KO) mice show disorganized hippocampal pyramidal neurons. The CA2/CA3 pyramidal cell layer is present as two abnormal layers and disorganized CA3 KO pyramidal neurons are also more excitable than wild-type (WT) cells. To further identify abnormalities, we characterized *Dcx* KO hippocampal neurons at subcellular, molecular and ultrastructural levels. Severe defects were observed in mitochondria, affecting number and distribution. Also, the Golgi apparatus was visibly abnormal, increased in volume and abnormally organized. Transcriptome analyses from laser microdissected hippocampal tissue at postnatal day 60 (P60) highlighted organelle abnormalities. Ultrastructural studies of CA3 cells performed in P60 (young adult) and > 9 months (mature) tissue showed that organelle defects are persistent throughout life. Locomotor activity and fear memory of young and mature adults were also abnormal: *Dcx* KO mice consistently performed less well than WT littermates, with defects becoming more severe with age. Thus, we show that disruption of a neurodevelopmentally-regulated gene can lead to permanent organelle anomalies contributing to abnormal adult behavior.

Keywords (10 max)

Cortical malformation, neurodevelopmental disorder, mouse knockout, hippocampus, molecular and cellular analysis, morphology, behavior, organelle, pyramidal neuron

1. Introduction

Human *Doublecortin* (*DCX*) mutations give rise to severe cortical malformations, the lissencephaly spectrum, associated with epilepsy and intellectual disability (desPortes et al., 1998; Gleeson et al., 1998; Bahi-Buisson et al., 2013). During cortical development, principal neurons are generated in deep regions of the brain and migrate long distances to reach the developing cortical plate close to the brain surface, where they grow axons and dendrites (Stouffer et al., 2016; Romero et al., 2018). In cases of lissencephaly it is thought that neurons become arrested during their migration, resulting in disorganized cortical layers and ectopically positioned neurons within the white matter. Abnormal positioning and integration of these neurons likely contributes to abnormal connectivity and function of the cortex.

Numerous gene mutations have been identified for these disorders (Di Donato et al., 2018), with a recognized involvement of the microtubule cytoskeleton, which is important for neuronal migration and differentiation (Francis and Cappello, 2021; Stouffer et al., 2016). *DCX*, one of the first lissencephaly genes identified, codes for a developmentally-regulated microtubule-associated protein (MAP, Francis et al., 1999; Gleeson et al., 1999; Sapir et al., 2000) known to nucleate and stabilize microtubules (Manka and Moores, 2020). The regulation of microtubules is critical in immature neurons: these cells undergo extensive changes of morphology requiring correct cytoskeletal dynamics, influencing organelle position and structure. Furthermore, leading processes, and growing axons and dendrites require the transport of organelles and cargos to distal regions of the cell (Lasser et al., 2018). Axons and dendrites, which can be extensively branched, generally have stable microtubule bundles to support transport, but are tipped with a growth cone exhibiting less stable, single microtubules. Regulators of microtubule behavior can hence contribute to neuron morphology, position and function.

Dcx, as well as other 'lissencephaly' genetic mouse models have been generated (Stouffer et al., 2016). Subtle microtubule and morphology defects in diverse populations of immature *Dcx* mutant neurons have been identified (Kappeler et al., 2006; Koizumi et al., 2006; Bielas et al., 2007; Tint et al., 2009; Liu et al., 2012). However, there are few obvious brain anatomical defects, with just the hippocampus showing a malformation (Belvindrah et al., 2014). *Dcx* mutants show perturbed CA2/CA3 pyramidal cell layer development, suggesting abnormal CA neuron migration, whilst the neocortex appears unaffected (Corbo et al., 2002; Kappeler et al., 2006). CA2/CA3 neurons are re-organized in two layers instead of a single layer as seen in control animals. *Dcx* mutant mice correspondingly show subtle behavioral defects, as well as neuronal hyperexcitability and epilepsy associated with the hippocampus (Corbo et al., 2002; Nosten-Bertrand et al., 2008; Bazelot et al., 2012; Germain et al., 2013). However, it is still unknown how the lack of *Dcx* expression during development

might lead to impaired adult neuron function. Assessing neurons at different stages of maturity could help identify mechanisms, potentially indicating new therapeutic strategies.

Characterizing CA pyramidal neurons during development in wild-type (WT) and *Dcx* knockout (KO) mice, we previously showed that the earliest-born CA2/CA3 neurons form an aberrant superficial layer (*stratum pyramidale* internal, SPI) in the postnatal brains of mutant mice, instead of being situated in the deepest part of the pyramidal cell layer (Khalaf-Nazzal et al., 2017). All subsequently generated neurons form a second deeper layer (*stratum pyramidale* external, SPE) below the SPI. Unexpectedly, transcriptional and ultrastructural analyses of early postnatal *Dcx* KO CA3 hippocampal neurons from both layers revealed abnormalities in mitochondria and Golgi apparatuses (GA, Khalaf-Nazzal et al., 2013), suggesting altered organelle function is a consequence of *Dcx* mutation. How such defects may impair the development and function of *Dcx* KO neurons, and/or contribute to their aging, remains unknown.

Using molecular, cellular and ultrastructural analyses, we sought here to investigate whether mitochondria and GA abnormalities contribute to abnormal neuron morphology, and if defects persist and affect function in the adult brain. Hippocampal neurons *in vitro* and *in vivo* exhibited mitochondrial and GA defects. Transcriptome data in postnatal day 60 (P60) microdissected hippocampal CA3 neurons also showed deregulated genes related to these organelles. At the ultrastructural level, comparing young (P60-P90) versus mature (7-10 months) CA3 cells, revealed persistent cellular defects. Complementing this work with behavioral tests showed that young and mature mutant animals were less active than WT mice, and memory defects were observed in fear conditioning tests. Impairments were observed more frequently in mature animals with KO mice being consistently worse than WT littermates. Overall these data reveal permanent organelle defects impacting hippocampal neuron function, not previously associated with a classical neurodevelopmental disorder.

2. Materials and Methods

Animals

Research was conducted according to national and international guidelines (EC directive 2010/63/UE, French MESR 00984.02) with protocols followed and approved by the local ethical committee (Charles Darwin, Paris, France). *Dcx* mutation was maintained by continuous backcrosses on the Sv129Pas genetic background. Mice were generated by crossing heterozygote (HZ) female with Sv129Pas male (Charles River, France). For all analyses hemizygote KO male mice were compared with WT littermate males.

Primary cultures of hippocampal neurons

The hippocampus was dissected from mouse E17.5 embryos in ice-cold 0.02 M HEPES in $\text{Ca}^{2+}/\text{Mg}^{2+}$ free HBSS (Gibco), and mechanically dissociated after incubation with trypsin (2.5 mg/ml). Only cultures with at least 1 WT and 1 *Dcx* KO were used. For all analyses, dissociated cells were plated on 14 mm-diameter coverslips (0.3×10^5 cells/ coverslip) coated with poly-L-lysine (0.05 mg/ml, Sigma) and cultured in Neurobasal medium supplemented with B27 (1%, Gibco), GlutaMAX (2 mM, Gibco), penicillin (100 units/ml) and streptomycin (100 mg/ml) at 37 °C in the presence of 5% CO_2 . Under these culture conditions (without using laminin as a substrate), the majority of neurons were polarized at DIV3, with extension of a single long neurite, and were optimally spaced in order for morphological and organelle analyses to be performed per cell. To label mitochondria, neurons were exposed to Mitotracker Red CMXRos (Invitrogen, 50 nM) for 30 min prior to fixation in PFA (4%) for 15 min.

***In Utero* Electroporation for *in vivo* analysis of Golgi apparatuses**

Timed-pregnant *Dcx* heterozygote mice (E13.5-E14.5) were anesthetized with isoflurane (4% during induction and 2%–2.5% during surgery), and the abdomen was opened to expose embryos within the intact uterine wall. Embryos were constantly hydrated with NaCl (0.9%). A solution containing DNA (1mg/ml per plasmid) and 20% w/v fast green in sterile endo-free water was injected in the lateral ventricle of the embryos. Two plasmids were used: pCAG-IRES-Tomato and pCAG-Galt-EGFP (a generous gift from Dr. Kimura and Dr. Murakami, (Kimura and Murakami, 2014). Forceps electrodes (System CUY650P5 NepaGene Co) were placed horizontally around the embryo head and plasmids were electroporated by discharging a 4,000-mF capacitor charged to 35 V (five electric pulses of 50 ms with 500 ms intervals) with a CUY21 NepaGene electroporator. The embryos were then placed back in the abdominal cavity. Cesarean section was performed at E19 if required, with use of a foster mother to rear the pups until P7-8, at which point the pups were deeply sedated by hypothermia and transcardially perfused with 4% paraformaldehyde in 0.1 M phosphate buffer, pH 7.4, for 5 min before brain removal. Brains were post-fixed overnight at 4 C.

Immunostaining and image acquisition

Primary neurons were incubated with blocking solution (5% normal goat serum, 0.2% Triton X-100 in 1X PBS) for 1 h at room temperature (RT), followed by incubation with primary antibodies for GM130 (BD Biosciences) and TUJ1 (RD Biosystems) in blocking solution for 2 h at RT or overnight at 4°C. Secondary antibodies (Invitrogen) were incubated in blocking solution combined with Hoechst for 60 min at RT in the dark. Coverslips were mounted with Fluoromount G (Southern Biotechnology). Neurons (TUJ1+) with non-overlapping processes were used for DIV3 morphology analyses. For analysis of tissue from IUE experiments

(brains collected at P7-8), 70 μm thick coronal sections were made using a vibrating blade microtome (Leica VT1000 S) and mounted with Fluoromount G without further immunostaining besides Hoechst. Neurons from all CA3 fields (CA3a-c) were pooled and used for analyses of Golgi apparatuses (GA).

Images (z-series) were acquired with a TCS Leica SP5-II confocal microscope using a 40X objective. Individually resolved MitoTracker-labeled elements were considered to be a single mitochondrion, regardless of size (e.g., Maes et al., 2017), which was measured in maximum projection images using the “analyze particles” function in ImageJ (Fiji) software, and reported as the average area per mitochondrion. GA volume was calculated using the anti-GM130 and/or GalT-EGFP fluorescent signal with ImageJ software using the 3D Objects Counter plug-in, which reports the individual volume of each object detected. Thus, the number of objects, which we termed GA ‘fragments’, represents how many discrete, labeled domains exist in 3-dimensional space, which we use as a means for gaining insight into GA structural differences during development and between genotypes. GA volume data is displayed as the total volume of all fragments per cell. GA length was measured *in vitro* using maximum projection images, drawing the smallest possible straight line covering the length of the GA located in the process (excluding the soma). For the *in vivo* analysis, z-series were oriented so that each apical and/or basal process was oriented perpendicularly in the z-dimension (with a zero degree angle) before measurements were made. For NPY immunostaining, 40 μm slices obtained from adult (8 weeks old) mice were incubated with blocking solution (10% normal goat serum, 0.5% Triton in 1X PBS) and for 1 h at RT, followed by incubation with an anti-NPY primary antibody (1:10,000; Sigma) overnight at 4°C in blocking solution. A secondary antibody (Invitrogen) was incubated for 1 h at room temperature. Hoechst staining (1:1000) was performed during the third wash. Slices were mounted with Fluoromount G and observed using a Leica DM6000 epifluorescence microscope. Images were acquired with the Metamorph software and cell counting was performed using ImageJ software.

Laser capture microdissection (LCM)

Coronal brain sections (12 μm) containing the rostro-caudal hippocampus were prepared using a cryostat (Leica) maintained at -20°C and mounted on PENmembrane slides (1440–1000, PALM, Bernried, Germany) which were pre-treated by RNase ZAP (Ambion) and UV irradiated in a cell culture hood for 30 min at 254 nm. After sectioning, the slides were stored in a -80°C freezer for use within 1 week. On the day of LCM, the slides were removed from the freezer, and fixed in 70% ethanol for 2 min, prepared in RNase-free water, and then in 50% ethanol for 5 sec, and stained with 1% cresyl violet (Sigma) for 1 min. Subsequently, slides were rinsed and dehydrated using serial dilutions of ethanol (50% for 5 sec, 75% for 5

sec, 100% for 30 sec). Sections were air-dried and subjected to LCM within the next 30 min. Samples were cut using a Zeiss LCM system (PALM Microbeam). In WT animals, the hippocampal CA3 region was microdissected in one piece. In *Dcx* KO animals, SPI and SPE CA3 cells in the two layers were separated. Per brain, the entire CA3 structure (bilateral) from the dorsal hippocampus was excised; for each condition 60 sections per animal (n = 5) were pooled.

RNA isolation, quantity and quality assessment

Total RNA was isolated from pooled microdissected material using an RNA isolation kit (Qiagen RNeasy microkit) according to manufacturer's instructions. RNA for each brain was eluted in 13 μ l of the elution buffer provided in the kit. RNA quantity was measured using a nanodrop spectrophotometer. RNA quality was checked using an Agilent 2100 Bioanalyzer with the RNA 6000 Pico LabChip Kit (5065-4473, Agilent Technologies, Palo Alto) according to the manufacturer's instructions. No statistical differences in RNA qualities ('RIN' values) were seen between the samples. One SPI RNA sample had a very low concentration and was hence excluded from further analysis.

Linear RNA amplification and GeneChip hybridization

14 samples, corresponding to n = 5 samples for WT and SPE and 4 sample for SPI were processed using the Illumina TotalPrep RNA Amplification Kit (Ambion, Life Technologies) and the Whole-genome Gene Expression Direct Hybridization Assay (Illumina) according to manufacturers' instructions. Briefly, 150–200 ng total RNA was used to prepare double-stranded cDNA using a T7 oligo (dT) primer (Illumina protocol). Reverse transcription was followed by *in vitro* transcription in the presence of biotinylated nucleotides. cRNA samples were hybridized to the Illumina Mouse-Ref-8 expression beadchip arrays in the appropriate buffer overnight at 58 °C. After hybridization and washes, fluorescent tagging was achieved by incubation with streptavidin-Cy3. Each array contains approximately 25,600 well-annotated RefSeq transcripts, represented as oligonucleotides attached to beads (average of 30 beads/per transcript), corresponding to over 19,100 unique genes.

Data analysis

Bead Chips were scanned on an Illumina iScan Reader using Illumina iScan control software version 3. Illumina Genome Studio software (version 2011.1) was used for preliminary data analyses. Quality controls were performed and analyzed with the Illumina Genome Studio software. The control summary report evaluates variations in signal intensity, hybridization signal, background signal, and the background/noise ratio for all the samples analyzed in each experiment. Quality controls (reference samples, principal component analyses before

and after normalization) showed neither batch nor BeadChip effect. Bead-averaged data were normalized using quantile normalization (BeadStudio software, Illumina, GmbH). The Illumina files were deposited in the GEO database under accession number GSE185031. Differential analysis per gene was performed using Student *t*-tests. The gene symbols corresponding to Illumina probe ids were retrieved with the Illumina Mouse-Ref8-v2 annotation data.

Gene ontology and cell type analysis

Analysis for enriched Gene ontology (GO) terms were performed with Database for Annotation, Visualization and Integrated Discovery (DAVID) Functional annotation Tool (v6.8) (Dennis et al., 2003). GO terms and pathways were considered as enriched for fold enrichment ≥ 2.0 , uncorrected *p* value ≤ 0.05 and minimum number of regulated genes in pathway/term ≥ 2.0 . A cell enrichment analysis for $P > 0.05$ lists was based on single-cell RNASeq data previously described in (Tasic et al., 2016). R software was used for cell type comparisons as described in Delahaye-Duriez et al., (2016).

qPCR analysis

cDNA was synthesized from 1 μg of RNA to which 1 μL of Random Primers at 300 ng/ μL and 1 μL of dNTPs at 10 mM were added. The mix was heated at 65°C for 5 minutes before 4 μL of 5X RT buffer from the SuperScript® IV First-Strand Synthesis System kit and 2 μL of 0.1 Dithiothreitol was added. The mix was left for 2 min at 25 °C before adding 1 μL SuperScript® IV RT. The mix was then left at 25 °C for 15 minutes, heated at 42 °C for an hour before inactivation of the enzyme by 15 minutes at 75 °C. According to this protocol, the ultimate cDNA concentration should be 50 ng/ μL . Gene expression was evaluated using the Stratagene Mx3000P® real-time (Agilent Technologies) according to MIQE guidelines (Bustin et al., 2009). Each reaction was made up of a 15 μL mix with 7.5 μL of SYBR® Green PCR Master Mix and 0.6 μL of a solution with the forward and reverse primers at a 5 μM concentration. The cDNA from the LCM was diluted 1:225 for a total concentration of 0.22 ng/ μL . Data analysis was performed using a variant of the $2^{-\Delta\Delta\text{Ct}}$ method (Livak and Schmittgen, 2001) and statistical significance was evaluated using a Student *t*-test unpaired for the WT to SPI or SPE comparisons and paired when comparing SPI to SPE.

Table 1. qPCR oligonucleotides.

Gene name	Gene ID	Forward primer	Reverse primer
Gabrb3	NM_001038701. 1	AAGGTGCCATGTTTTCTGAA	ATGGTGCATGAGCCACTCTG

Camk2a	NM_177407	TGGAGACTTTGAGTCCTACACG AA	AAAGGCTGTCATTCCAGGGTC
Rcan2	NM_207649	GACCTCCCAGCATCGAGAAAG	AGAGCGCTAAAGAGGTTTGCAT
PtgDs	NM_008963	CGAGCTGAAGGAGAAATTCACC	CCTGCGTTTACTCTTGAATGCA
Dbi	NM_007830	CAAGTGGGACTCGTGGAAACAA	TCCACATAGGTCTTCATGGCAC
Npy	NM_023456	GCTCTGCGACACTACATCAATC TC	AGGGCTGGATCTCTTGCCATA
Olig1	NM_016968	CGTCTTGGCTTGTGACTAGCG	GCCAGTTAAATTCGGCTACTGT C
Eif4a2	NM_013506	ATCAGGGTCAAGCCGTGTTCT	ACTTGTTCACGTCAATCCCA
Atp5b	NM_016774	GTGCCCTTGAAGGAGACCATTA	GCTTGTTCGGGAGATGGTCA
Psap	NM_011179	CTGGTGTGACAACATGGAGACT G	TGACTTCTGCAGCTGGGAAA
Cyp	NM_001356326	CCA TCG TGT CAT CAA GGA CTT	TTC CCA TCC AGC CAG GAG GTC
Mfn1	NM_024200	Sigma ; Proprietary	Sigma ; Proprietary
Aldoc	NM_009657	Sigma ; Proprietary	Sigma ; Proprietary

Electron microscopy (EM) and morphometry

Mice for EM (for young adults (4weeks +/- x) 3 KO and 3 WT from 3 different litters were used; for mature adults (8 +/- 1 months) 5 KO and 4 WT from 3 different litters were used) were perfused with 4 % PFA and 2.5 % glutaraldehyde in 0.1 M phosphate buffer (PB). The brains were removed and placed in fresh fixative overnight at 4°C and rinsed in PB. Vibratome sections were performed across the CA3 hippocampal region and postfixed in 2% OsO₄ (in PB), dehydrated in an ascending series of ethanol, and embedded in epoxy resin. Semi-thin sections (0.5 μm) were stained with toluidine blue and images were acquired with a Coolsnap CCD camera mounted on a Provis Olympus Microscope. Ultra-thin sections (40 nm) were mounted on either 200 mesh or one slot grids, cut and double stained with uranyl acetate and lead citrate prior to observation with a Philips (CM-100) electron microscope. Digital images from the CA3 region were obtained with a CCD camera (Gatan Orius). Analyses was performed with the software Digital Micrograph.

For each animal, two independent series of sections were generated and quantified by two blind observers: one series for Golgi analyses and the nucleus; the other series was used to quantify damaged mitochondria, lysosomes in the cytoplasm, lipofuscin vesicles, nuclei and nucleoli in the nucleus. Nuclei data were equivalent and pooled from the two series. All visible full cells (perinuclear region only) per section were quantified: For young and mature adults, a total of 53-138 cells were quantified for WT, 39-155 SPE cells and 42-113 SPI cells for KO mice.

Cyclotron test

The horizontal (locomotion) and vertical (rearing) activities were individually assessed for 30 minutes in transparent cages with automatic monitoring of photocell beam breaks (Imetronic, Bordeaux, France).

Open-field test

Open field tests were performed in a chamber (50 cm × 50 cm) equipped with infrared sensors (CCTV lens) in a room with high light (100-150 lux). Mice could freely explore the novel environment for 9 min, and their activities were video-tracked and automatically recorded using Viewpoint application manager software (VideoTrack 3.10).

Fear conditioning (adapted from (Penzo et al., 2015; Wille et al., 2015))

The experiment took place in a sound attenuated cage (Imetronic). Before each conditioning session, the test cage was wiped clean with 70 % ethanol. During conditioning, the cage was illuminated and the behavior was captured with a monochrome camera. Once placed in the chamber, the mice were allowed to explore the context for 2 minutes of habituation, and then were exposed to the pairing of a tone as conditioned stimulus (CS, 30 s tone stimulation, 80 dB, 4 kHz), which co-terminated with a 2 s, 0.6 mA foot shock (US, unconditioned stimulus) (CS/US), and mice were left in the cage for 2 min post-CS/US. The test for contextual memory was performed 24 h following conditioning in the same context for 5 minutes. To assess memory for the CS, 48 hours after the conditioning session, mice were placed in a novel context for 2 minutes, then exposed to presentations of the CS for 2 minutes. The novel context was a cage with a differently textured floor and walls compared with the conditioning cage. Prior to each use the floor and walls of the cage were wiped clean with 0.5 % acetic acid to make the scent distinct from that of the conditioning cage.

Statistical Analysis

All statistical analyses were performed using Prism (Version 9.2.0 Graph Pad, USA). For variables that follow a normal distribution, data were subjected to factorial two- to 3-way analysis of variance (ANOVA), with CA3 layers, genotype, age and position in the cell as between-group main factors. Significant main effects were analyzed further by *post hoc* comparisons of means using Student's, Tukey's or Sidak's tests (see Supplementary data tables). For other variables, statistical analyses were carried out using nonparametric tests. The Mann–Whitney rank sum test was used to compare quantitative variables between two groups and proportions were compared using the Chi-squared test (χ^2). Only significant statistical tests are reported in the text, with the significance established at a P-value < 0.05.

3. Results

Altered mitochondrial number in immature Dcx KO pyramidal neurons

Immature *Dcx* mutant hippocampal neurons were previously demonstrated to exhibit altered branching complexity *in vitro* (Bielas et al., 2007; Tint et al., 2009) and more mature CA3 neurons *in vivo* showed decreased dendritic lengths (Bazelot et al., 2012). Mitochondrial trafficking and distribution has been shown to regulate dendritic branching during development and neurodegeneration (Kimura and Murakami, 2014; Faits et al., 2016; López-Doménech et al., 2016). We therefore investigated neuron morphology and mitochondrial characteristics in WT and *Dcx* KO immature hippocampal neurons at 3 days *in vitro* (DIV3), labeled with Mitotracker. Neurons at this stage have one main, long process and multiple shorter processes extending from the soma, the stage at which previous *in vitro* studies (DIV1-5) found morphological abnormalities.

First assessing morphology, we found no significant differences between *Dcx* WT and KO DIV3 neurons in branching complexity and total process length (**Supplementary Fig. 1A, B**). However, the total number of mitochondria located in neurites per cell was significantly decreased in KO compared to WT neurons (**Fig. 1A, B**). Because the number of mitochondria may vary depending on the hierarchy of tree processes, we assessed their number in the different types of process. Both WT and KO neurons showed more mitochondria in main compared to the somal processes, with KO neurons having significantly less mitochondria in both main and somal processes (**Fig. 1C**). Furthermore, mitochondria are often associated with process branch points (Faits et al., 2016). In *Dcx* KO neurons the percentage of mitochondria-containing branch points was decreased compared to WT neurons (**Fig. 1D**).

These combined results may suggest that mitochondrial production, viability, trafficking and/or tethering are impaired in *Dcx* KO neurons. We next assessed mitochondrial size, which is known to be dynamically regulated by fission and fusion, and is variable in mature neurons with respect to location in the axon or dendrites (Chen and Chan, 2009). We found that mitochondrial size was not altered in *Dcx* KO neurons (**Fig. 1E**), indicating that fission and fusion dynamics are unlikely to be modified, and that compartment-specific mitochondrial characteristics are not yet acquired at this early stage.

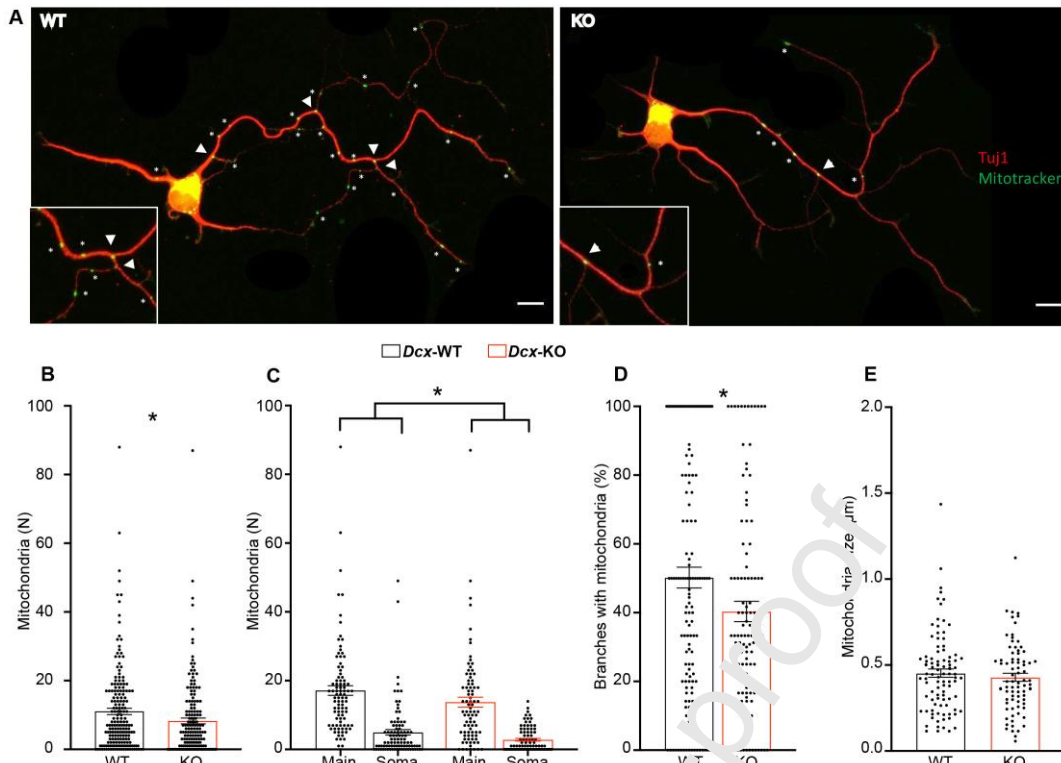


Figure 1. Decreased mitochondria and altered distribution in *Dcx* KO primary hippocampal neurons. (A) WT (left) and KO (right) primary hippocampal neurons at DIV3 labeled with Tuj1 (microtubules, red), mitotracker (green) showing mitochondria located in neuronal processes (asterisk *) and at branch points (arrowheads). Scale bar = 10 μ M. (B) The total number of mitochondria in all processes per cell was significantly decreased in KO neurons compared to WT (Student's test: $t(356) = 2,193$, $p = 0.029$). (C) The decreased number of mitochondria in KO neurons was observed both in main and somal processes: the main process is defined as the longest neurite and somal processes are all other neurites originating from the soma, as described previously (Bielas et al., 2007). (ANOVA: Genotype: $F(1, 354) = 6.27$, $p < 0.0127$; Position: $F(1, 354) = 109.3$, $P < 0.0001$; G x P interaction: ns, $p = 0.6$). (D) The percent of branch points exhibiting mitochondria was significantly decreased in KO neurons compared to WT ($t(41) = 2.305$, $p = 0.022$ test). (E) Size of mitochondria (μ m) located in neuronal processes is not different between genotypes ($t(169) = 0.7127$, ns). N = 85-92 neurons from 8-9 embryos from 4 cultures per genotype. * $p < 0.05$.

Altered GA orientation in immature *Dcx* KO pyramidal neurons

Structural changes in microtubules were previously observed in *Dcx* KO neurons (Bielas et al., 2007). Microtubules are also known to play a role in the organization and orientation of the GA. In neurons, the GA orients toward the longest dendrite, and this polarity precedes asymmetric growth of the primary dendrite (Horton et al., 2005). We therefore decided to assess somatodendritic GA structure in developing WT and *Dcx* KO neurons using the *cis*-GA marker GM130 (Horton et al., 2005; Thayer et al., 2013).

We first observed an increase in the apparent size of the GA in KO compared to WT neurons. At DIV3, the GA was compact and often present in 1-2 continuous globular fragments (Supplementary Fig. 2A), with no difference in the number of fragments between

genotypes ($p = 0.6$; Fisher's exact test). GA volume was not significantly greater in *Dcx* KO neurons compared to WT at DIV3 (**Supplementary Fig. 2B**), but became significant in neurons at DIV9 (**Fig. 2 A, B**). As neurons matured in culture, the GA increased in size and complexity, with an increased percentage of KO neurons having a more fragmented GA (defined here as having ≥ 10 detectable GA fragments; **Fig 2C**) but there was no significant increase in the overall number of GA fragments between genotypes (**Supplementary Fig. 2C**). At DIV9 the GA was sometimes observed to protrude into a single process (**Fig. 2 A**) as described previously (Horton et al., 2005), but the length of this protrusion was not significant between genotypes (**Supplementary Fig. 2D**).

Next, we performed *in utero* electroporation (IUE) in the hippocampus at E13-14 to label the GA in CA3 pyramidal cell neurons *in vivo* using the trans-GA marker GalT (Kimura and Murakami, 2014). Mice were sacrificed at P7-8 to analyze CA structure and orientation in immature hippocampal CA3 neurons in brain slices (**Fig. 2D**). There were no discernable differences in the number of discretely labeled GA fragments and GA volume between genotypes in these analyses (**Supplementary Fig. 2 E, F**). Most neurons showed the GA invading one apical process, and the proportion of apical processes with GA was also not different between WT and KO (**Fig. 2E**). The length of the GA invading the apical dendrite was not significantly increased in KO cells (**Fig. 2F**). Unexpectedly, we also observed that the GA could invade basal processes with 42 % WT neurons showing basal dendrites with GA (grey shaded bars in **Fig. 2G**). This percentage was reduced to 21 % in KO (**Fig. 2G**). Thus, KO neurons mostly lacked GA in basal processes at this age. This suggests changed GA dynamics during dendrite development, which may contribute to structural and functional defects in the adult.

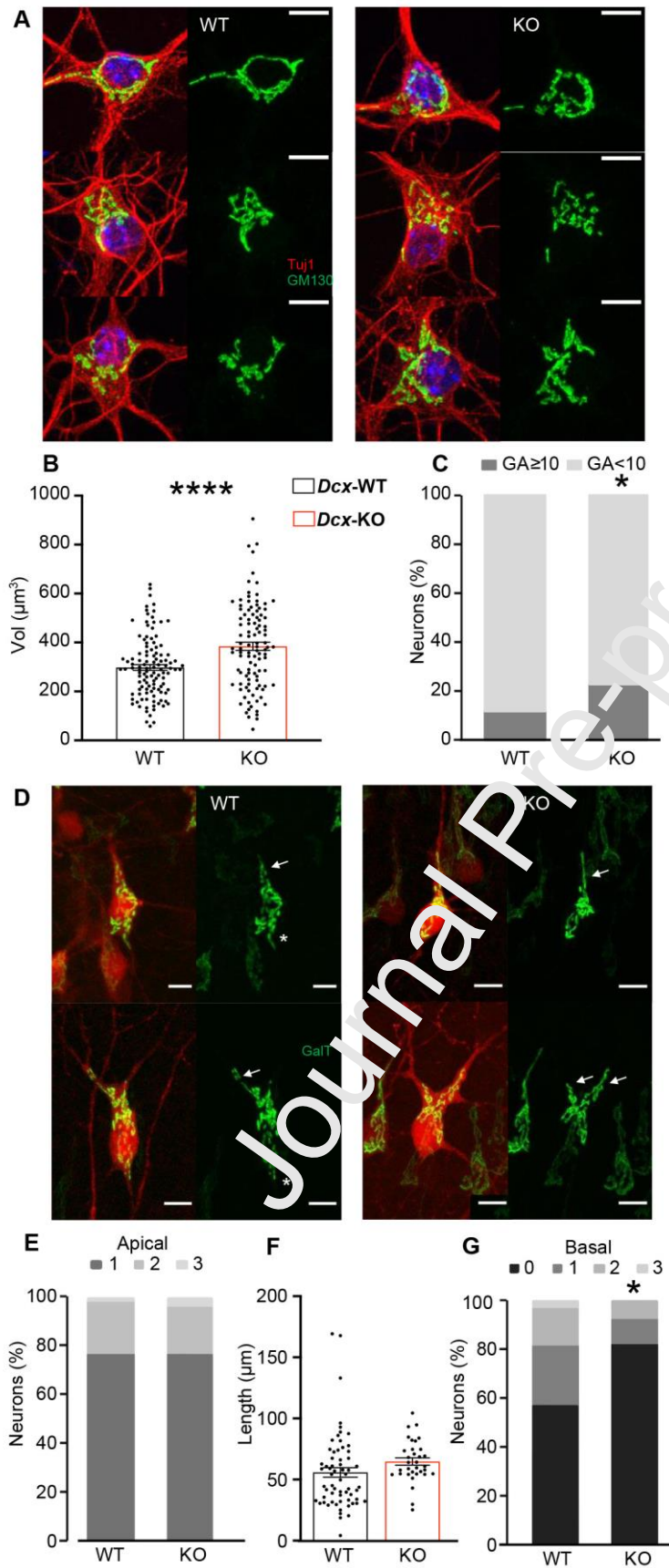


Figure 2. Altered Golgi apparatus size and shape in *Dcx* KO hippocampal neurons. (A) WT (left) and KO (right) primary hippocampal neurons at DIV9 labeled with Tuj1 (microtubules, red), GM130 (GA, green), and DAPI. Scale bar = 10 μM . **(B)** GA volume was

greater in *Dcx* KO neurons at DIV9 compared to WT (**** $p < 0.0001$; *t* test, $n = 105-114$ neurons from 5-6 embryos from 3 cultures per genotype). **(C)** There was an increased proportion of *Dcx* KO neurons at DIV9 with ≥ 10 GA fragments (* $p = 0.0238$, χ^2). **(D)** WT (left) and KO (right) hippocampal neurons at P7-8, which were labeled by *in utero* electroporation at E13.5-14.5 with pCAG-GalT-GFP (GA, green) and pCAG-Tdtomato (cytoplasmic, red). Arrows and asterisks indicate apical and basal processes that contain GA, respectively. Scale bar = 10 μM . **(E)** Distribution of GA into apical processes was quantified with no differences detected between the genotypes (χ^2 , distinguishing number of processes 1,2 and 3, apical ns, $n = 66$ WT, 33 KO neurons from 3 litters with 5 WT and 3 KO mice). **(F)** The longest length of the GA protrusion into apical processes was not altered in *Dcx* KO neurons (Student *t*-test ns). **(G)** Distribution of GA into basal processes was quantified, and there was a significantly greater proportion of basal processes containing GA in WT CA3 neurons (χ^2 distinguishing number of processes ≥ 2 , basal * $p = 0.0351$, $n = 66$ WT, 33 KO neurons from 3 litters with 5 WT and 3 KO mice).

Molecular analyses confirm organelle defects at P60

We next decided to assess molecular changes in adult hippocampal KO neurons. In accordance with a previous transcriptome study performed in CA3 hippocampal tissue at P0 (Khalaf-Nazzal et al., 2017), revealing disrupted mitochondrial and GA gene expression, we applied a similar approach at P60. We first used laser capture microdissection of CA3 pyramidal neurons, separating in the KO the internal (SPI) from the external (SPE) layer, and dissecting the comparably well-organized CA3 layer from WT tissue (**Fig. 3A**). By comparing SPI and SPE separately to WT, this approach allowed us to determine if molecular changes evolved differently over time in the two KO layers, which seemed plausible given the structural differences between SPI and SPE neurons (Bazelot et al., 2012) and their different birthdate identities (Khalaf-Nazzal et al., 2017). Differentially expressed genes were identified by hybridizing prepared RNAs to Illumina arrays and searching for KO deregulated genes (**Supplementary Tables 1-3**). 1570 transcripts were significantly deregulated ($P < 0.01$, ratio > 1.1) in SPI compared to WT, whereas 141 transcripts were deregulated in SPE (**Supplementary Table 1**). Comparing SPI and SPE results, 1050 transcripts overall were upregulated compared to WT (with 41 common to SPI and SPE, **Fig. 3B**). Similarly, 661 transcripts were downregulated in SPI and / or SPE (with 34 in common). The highest changes amongst the commonly deregulated SPE and SPI genes ($P < 0.01$, ratio 1.2 compared to WT) are also shown (**Supplementary Table 3**), revealing a number of deregulated trafficking and organelle proteins common to KO cells. We further compared SPI to SPE revealing 826 transcripts showing deregulation (**Supplementary Table 2**). To validate this transcriptome screen, 10 genes were tested by RT-qPCR and showed similar trends (up or down-regulation) compared to the microarray analyses (**Supplementary Fig. 3A; Supplementary Table 4**).

Gene ontology (DAVID) analyses were performed to identify major functional categories involving the deregulated transcripts (**Supplementary Table 5**). As shown for SPI versus WT (**Fig. 3C,D**), SPE versus WT and SPI versus SPE (**Supplementary Fig. 3 B-D**), significant categories often correspond to organelles or cellular compartments (e.g. ribosome, mitochondrion, lysosome, endosome, GA and membranes), or identify processes such as enzyme binding, protein localization, binding and degradation, translation and vesicle-mediated transport. Similar categories were identified previously in both *Dcx* KO cell layers at P0 (Khalaf-Nazzal et al., 2017). Concerning over 100 deregulated mitochondrial genes, citing examples, 13 *Ndof*, 2 *Cox* and 12 *Atp* genes are present in the SPI versus WT list (**Supplementary Table 2**, see also **Supplementary Table 6** for those up and down regulated). Concerning GA-related genes, *Golm*, *Golga*, *Coq*, *Sys1*, *Gorasp1* and *Ergic* family members are also represented (**Supplementary Table 2**). SPE gene lists also show deregulated mitochondrial and GA-related genes (**Supplementary Table 2 and 6**). The numerous organelle gene deregulations suggest structural, functional and/or trafficking abnormalities in KO cells.

To help characterize SPI and SPE, we performed a cell enrichment analysis based on single-cell RNASeq data previously described in (Tasic et al., 2016). The subsequently identified enriched cell types found by this analysis of the SPI gene lists indicate a less-pure CA3 pyramidal cell population than expected, likely due to the nature of this thin pyramidal cell layer embedded in the mature *stratum radiatum* (**Supplementary Fig. 3E**). Amongst non-neuronal cells, genes corresponding to oligodendrocytes, microglia, astrocytes, endothelial and mural cells were also identified, as well as interneuron genes. The same analysis performed for SPE differentially expressed gene lists revealed that interneurons were the only significantly enriched contaminating cell type (**Supplementary Fig. 3E**). Laser microdissected SPE and WT CA3 neuron populations are thus relatively similar in composition.

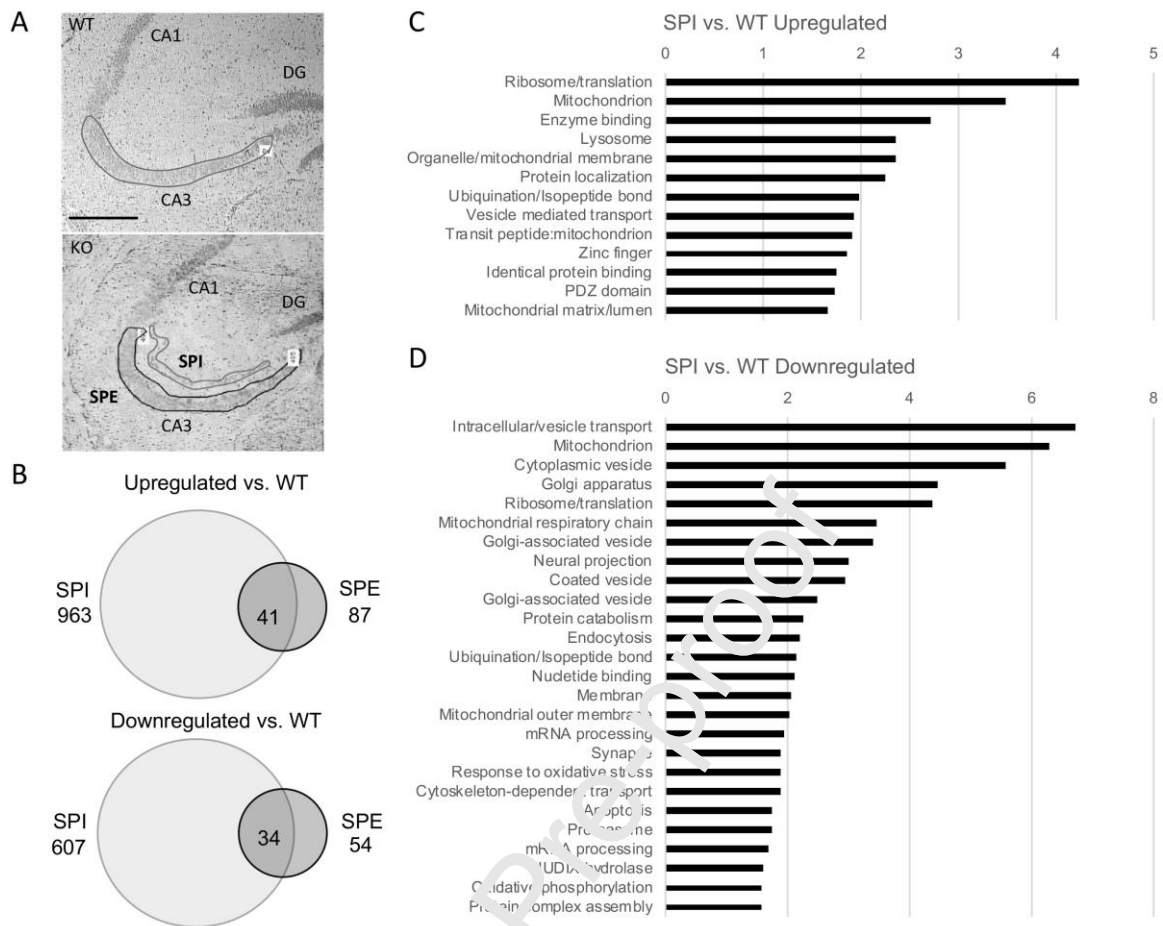


Figure 3. Dysregulated genes in SPI and SPE corresponding to organelle gene ontologies (A) Laser capture microdissection from cresyl violet stained P60 brain sections. Hippocampal CA3 WT (top) and *Dcx* KO (bottom) SPI and SPE layers are shown with schematized indications of areas selected for excision (scale bar 300 μ m). **(B)** Venn diagrams showing the number of transcripts up- or downregulated in *Dcx* KO SPI and/or SPE CA3 hippocampal pyramidal cell layers compared to WT (genes with $p < 0.01$, ratio > 1.1). DAVID functional clustering of SPI versus WT up- **(C)** and down-regulated **(D)** gene expression differences (transcripts with $p < 0.01$). Each significant functional category (y-axis), is plotted against the value of enrichment score (x-axis).

Having identified neuropeptide Y (NPY) amongst deregulated SPI genes **(Supplementary Fig. 3A)**, we used immunostaining to compare the proportion of NPY-positive cells in different regions. Abnormal distribution was observed in the KO *radiatum*, *pyramidale* and *oriens* strata **(Supplementary Fig. 3F, G)**. Within the pyramidal cell layers, there were many more NPY+ cells associated with SPI compared to SPE **(Supplementary Fig. 3H)**, in fitting with transcriptome results (NPY was not found deregulated in SPE versus WT, **Supplementary Table 2**).

Overall, gene expression analyses indicate organelle abnormalities in both SPI and SPE, although some gene perturbations (especially in SPI) may be derived from contaminating cell types.

Comparison between P0 and P60 transcriptome dysregulation

We noted amongst P60 genes, how many were in common with P0 data in order to understand how organelle and other potential abnormalities changed with neuron maturation (**Supplementary Table 7**). In SPE, 14.3 % (12) of the 84 upregulated genes at P60 were in common and 12.5 % (6) of the 48 downregulated genes were in common. In SPI, 17 % (156) of the 916 P60 upregulated genes were in common with P0 and 12 % (65) of the 538 downregulated genes were in common. Thus 12-17 % of P60 deregulated genes were already present in P0 deregulated gene lists.

According to NeXtprot (<https://www.nextprot.org/>), of the 12 common upregulated SPE genes, the majority are apparently related to organelles (peroxisomal *Dhrs7b*; nucleolar *Nol4*, *Zcchc17*; vacuolar *Vps24*; mitochondrial *Mterfd2*, Golgi *Gcat2*, *Pgpep1*), and some are involved in ubiquitination (*LOC545056*, *Keap1*, the latter also an anti-oxidant), or microtubule function (*Map1lc3b*). Two are involved in transcription / RNA processing (*D6Wsu163e*, *Traf1*). Thus, these upregulated genes largely seem to reflect the abnormal organelles and / or cell stress likely to be present.

Of the 6 common SPE downregulated genes, these appear to have quite varied functions (one is actin-binding (*Coro1a*), another a nuclear intermediate filament (*Lmna*), one is an enzyme related to lysosomal degradation (*Nagk*) and one a ribonuclease (*Rnaset2b*). The other 2 genes indicate the consistent interneuron contamination of this population at both time points (e.g. *Pvalb* and *Igsf21*).

We note that several common genes apparently upregulated in SPI correspond to predominately interneuron, astrocyte or oligodendrocyte genes (e.g. *Olig1*, *Pdgfra*), in fitting with the identified contamination of this pyramidal cell population at both ages studied. Functional annotations show that 66 (42 %) of SPI upregulated genes are apparently related to membrane proteins (e.g. there are members of tetraspanin, potassium channel, tight junction, cell adhesion, receptor, transporter, solute carrier, glycoprotein, Rab, neurexin and semaphorin families). Some also associate with the GA. Notably as well there were 16 secreted, 19 extracellular and 21 genes involved in transport. Functional annotation clusterings reveal glycoproteins, lipoproteins and cell adhesion as top categories. Certain common SPI upregulated membrane genes furthermore identify the deep layer neuronal population, e.g. *Hcn2*, coding for a hyperpolarization-activated channel.

Of the 65 common SPI downregulated genes, 9 are transcription / RNA binding, 6 are mRNA processing factors and 23 code for membrane related (10 transport) proteins. Examples are neurexin 1 (*Nrxn1*) and adaptor complex μ 1 (*Ap1m1*). The latter are also sometimes associated with the endoplasmic reticulum and GA (e.g. *Trappc3/c4*) or mitochondria (*Mtx1*, *Tom34*). Interestingly, plasma membrane presenilin enhancer protein (*Psenen*), synuclein (*Snca*) and amyloid beta precursor (*Apba2*) genes are also present,

which are related to neurodegenerative diseases. *Spg21* involved in spastic paraplegia is also in this list. Other commonly downregulated genes are related to the cytoskeleton, ubiquitination and/or the proteasome (*Nub1*, *Psmb7*), neddylation (*Dcun1d2*), the chaperone system, calcium modulation (*Cam1*) and other signaling, metabolism and anti-oxidant (e.g. *Vkorc1l1*) proteins. It may be interesting to re-increase their expression to assess the effect on neuron function. However, contaminating cell types, particularly in SPI, likely contribute to deregulated genes and should first be confirmed by histology.

Of particular interest are the persistently deregulated genes that are exclusively expressed in pyramidal neurons (according to the Allen Brain Map Mouse Transcriptomics Explorer, https://celltypes.brain-map.org/rnaseq/human_m1_10x) and are known to regulate synaptic plasticity, including *Gria2*, *Grasp1*, *CamK2a* and *Slc6a7*. GluA2 subunits (*Gria2*) regulate calcium permeability of AMPA receptors, and are thus important for synaptic plasticity and learning. *GluA2* KO mice demonstrate increased LTP in the CA1 region as well as behavioral deficits (Jia et al., 1996). Recently *de novo* variants in *GRIA2* have been associated with neurodevelopmental disorders and epilepsy in human patients (Salpietro et al., 2019). *Gripap1* (*Grasp1*) is an endosomal protein that is also involved in regulation of AMPA receptor trafficking, and *Grasp1* KO mice demonstrate impaired learning-dependent synaptic plasticity and behavior (Chiu et al., 2017). *Camk2a* is a calcium/calmodulin-dependent protein kinase that is crucially involved in regulating synaptic plasticity of glutamatergic receptors (Hell, 2014). *De novo* mutations identified in patients with intellectual disability can lead to an increase or decrease in CAMK2 auto-phosphorylation (Küry et al., 2017). Finally, *Prot* (*Slc6a7*) is a transporter for L-proline, an amino acid found prevalently in the brain, which can regulate glutamatergic transmission (Schulz et al., 2018). *Prot* KO mice show changes in glutamatergic biochemistry and behavior (Schulz et al., 2018). Patients with hyperprolinemia (inability to metabolize proline) demonstrate epilepsy and intellectual disability (Raux et al., 2006). Therefore, deregulation of these genes may contribute to hyperexcitability and epilepsy phenotypes previously related to the abnormal *Dcx* KO hippocampus, and may even provide targets for genetic or pharmacological intervention.

Abnormal ultrastructural organization in adult *Dcx* KO CA3 neurons at two adult ages

Electron microscopy (EM) characterization of early postnatal P0 *Dcx* KO CA3 layers was previously performed, revealing organelle defects (Khalaf-Nazzal et al., 2013). Here we questioned the outcome of ultrastructural abnormalities with aging by comparing young adult (2-3 m) to mature (7-10 m) adult WT and KO hippocampi. CA3 pyramidal cell layers were

identified in coronal semi-thin sections from WT and *Dcx* KO littermate mice. Pyramidal neuron-like somata were recognized by their large nuclear size, clear cytoplasm and compact organization into a single monolayer in the WT, or as internal (SPI) and external (SPE) layers in the KO, as described previously (Khalaf-Nazzal et al., 2013; Khalaf-Nazzal et al., 2017).

At P0, structurally abnormal and swollen mitochondria were observed in both *Dcx* KO CA3 layers, but not in WT neurons (Khalaf-Nazzal et al., 2013). In young adult mice, we observed that mitochondrial abnormalities were present at low frequency in WT, but more frequent in the KO CA3 (**Fig. 4 A-C**). Interestingly, this was particularly the case for the SPE layer, which showed significantly more defects, compared to WT (and SPI (**Fig. 4C**)). All statistical data for ultrastructural experiments are resumed in **Supplementary Table 8**. Abnormalities are increased with aging, with notably an increase observed in mature SPI compared to WT (and mature SPI compared to young SPI), reaching almost equivalent levels to the defects detected in mature SPE. We further checked the number of mitochondria per soma. Interestingly, in young adults, the number was significantly reduced in SPI somata compared to the WT layer (**Supplementary Fig. 4A**). Numbers in both mature SPE and SPI compared to mature WT were not significantly different.

Somata of both CA3 layers exhibited modified GA structure compared to WT at P0 (Khalaf-Nazzal et al., 2013). In both young and mature adult neurons, we also observed increased GA alterations in cells from both *Dcx* KO layers compared to WT (**Fig. 4 D-F**). These alterations did not significantly alter with aging. We also compared the numbers of GA stacks detected per cell. In young adults, these were significantly increased in both KO layers compared to WT (**Supplementary Fig. 4B**), but then increased with age only in WT mice.

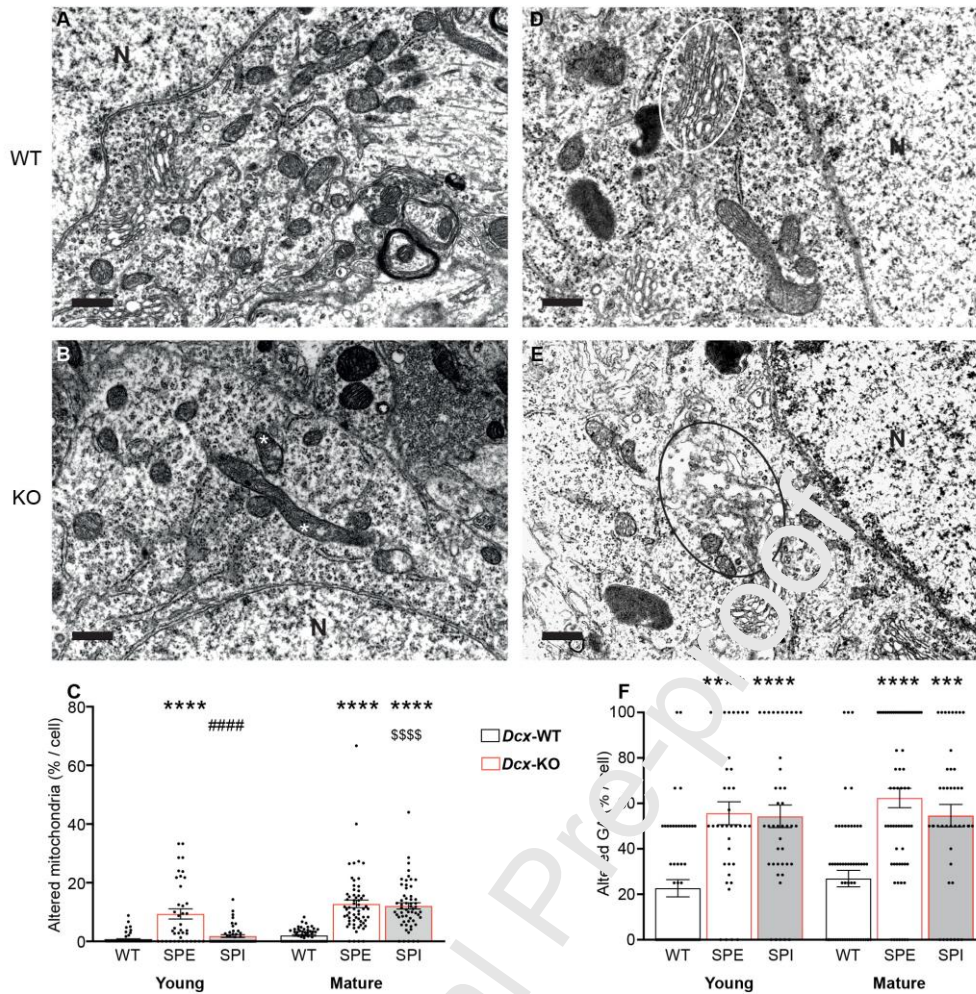


Figure 4. Altered mitochondria and Golgi apparatus in *Dcx* KO CA3 neurons.

(A,B) High magnification electron micrographs of hippocampal CA3 pyramidal neurons illustrating normal (A) or altered (B, white asterisk) mitochondria in WT and *Dcx* KO mice respectively. (C) Quantitative analyses showing that altered mitochondria (% per cell) significantly differ between CA3 layers and their percentage increased with aging, but differently according to the layers (ANOVA: CA3 Layer, $F(2, 312) = 50.97, p < 0.0001$; Age: $F(1, 312) = 39.68, p < 0.0001$, L x A interaction: $F(2, 312) = 11.63, p < 0.0001$). (D,E) High magnification EM of hippocampal CA3 pyramidal neurons illustrating normal (D) or altered (E) Golgi apparatus in WT and *Dcx* KO mice respectively. (F) Both SPE and SPI KO CA3 layers exhibited more altered GA compared with WT, but GA alteration did not worsen with age (ANOVA: CA3 Layers, $F(2, 293) = 37.42, p < 0.0001$; Age: $F(1, 293) = 1.056, ns$; L x A interaction: $F(2, 293) = 0.2449, ns$). Values represent means \pm SEM. Scale bars: A,B,D,E, 0.5 μ m. * vs WT, # vs SPE and \$ vs Young. *** < 0.001 , **** < 0.0001 .

Also at P0, nuclei in SPE possessed altered shapes and were less well aligned than SPI and WT nuclei (Khalaf-Nazzal et al., 2013). In adult mice, nuclear diameter also differed, more severely affecting SPI than SPE (Fig 5 A-D). Thus, in young adults, nuclear diameter was significantly smaller in the *Dcx* SPI compared to both WT and SPE layers. Nuclear diameter decreased with age in both KO layers, but not in WT. Once again, nuclear diameter was smaller in SPI compared to SPE KO layers. We also observed that nucleoli size was

altered, most severely affecting SPI (**Supplementary Fig. 4**), not previously shown in relationship with *Dcx* mutation.

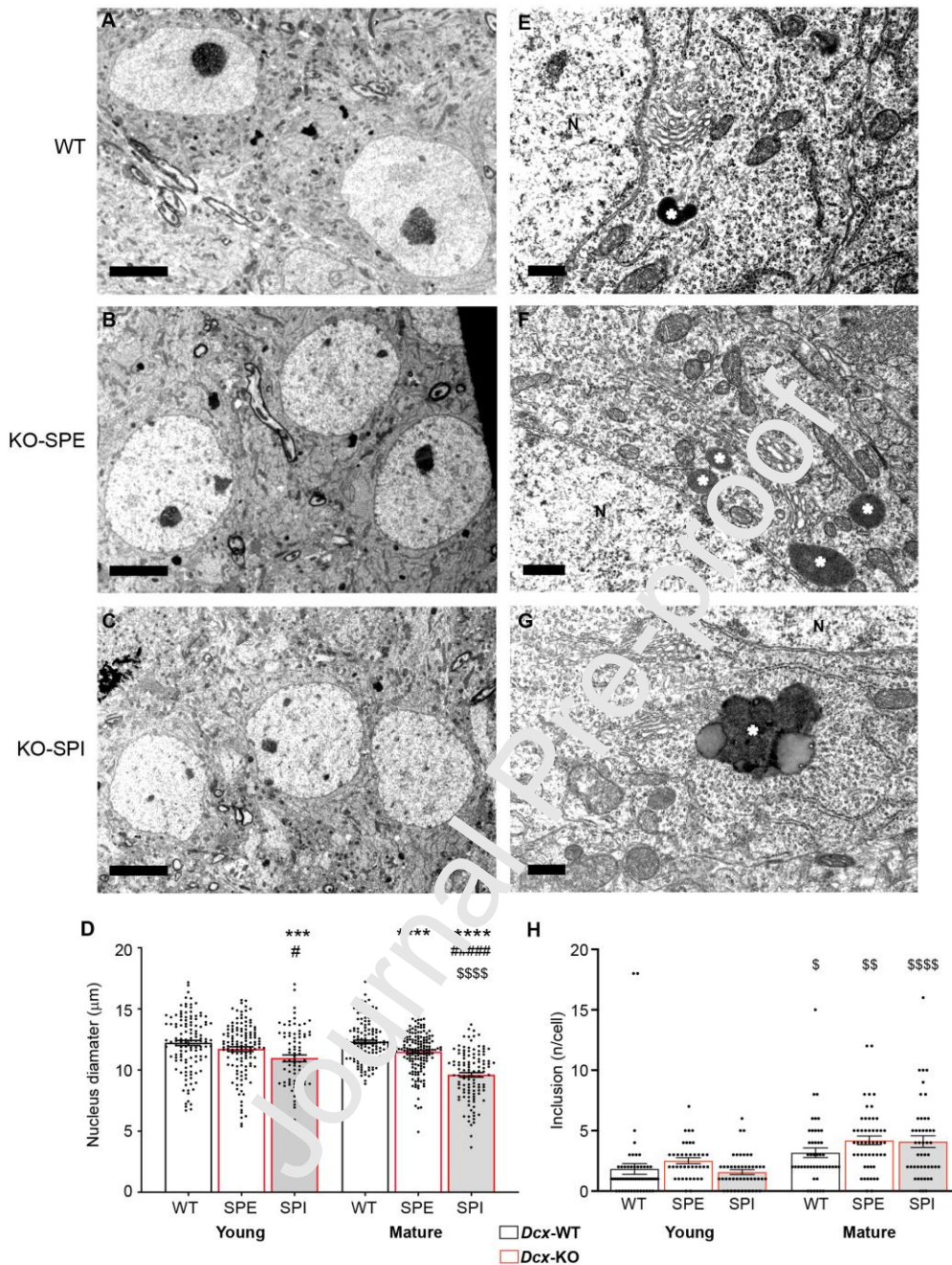


Figure 5. Reduced nucleus diameter of hippocampal CA3 pyramidal neurons with aging is more severe in *Dcx* KO SPI layer.

(**A-C**) Low magnification electron micrographs of hippocampal CA3 pyramidal neurons illustrating nuclear diameter in WT (**A**), KO-SPE (**B**) and KO-SPI (**C**) layers. (**D**) Nuclear diameter significantly differed between CA3 layers and decreased significantly with age, but in interaction with CA3 layers (ANOVA: CA3 Layers, $F(2, 728) = 52.3$, $p < 0.0001$; Age: $F(1, 728) = 10.95$, $p = 0.001$; L x A interaction: $F(2, 728) = 7.342$, $p < 0.0007$). At both ages, SPI exhibited smaller nuclei compared to WT and SPE layers. No decrease in nuclear diameter with age was observed in WT, and the decrease was more pronounced for SPI compared to the SPE layer. (**E-G**) High magnification electron micrographs of hippocampus CA3 pyramidal neuron illustrating lipofuscin inclusions (**E,F**) and lipofuscin inclusions containing clear areas resembling lipid droplets (**G**). (**H**) The number of inclusions increased with age

(ANOVA: Age: $F(1, 279) = 34.96, p < 0.0001$), with a limited effect of the CA3 region (SPI or SPE) to the significance (ANOVA: CA3 Layer: $F(2, 279) = 2.5, p = 0.0839$; L x A interaction: ns): however, there were no significant differences in the number of inclusions in the SPE and SPI layers compared to the WT layer. Values represent means \pm SEM. * vs WT, # vs SPE and \$ vs Young. * < 0.05 , ** < 0.01 , *** < 0.001 , **** < 0.0001 .

We furthermore quantified lipofuscin inclusions (**Fig. 5 E-G**), which are a type of intracellular protein aggregation that accumulates during aging (Keller et al., 2004). In all CA3 layers, the number of inclusions per cell increased with aging, with a non-significant ($p = 0.08$) increase in KO compared to WT layers (**Fig 5H**).

Thus, ultrastructural analyses of CA3 neurons reveal organelle defects in *Dcx* KO neurons at both ages examined, with these being consistently detected in mature cells.

Impaired context and cued memory in both young and mature *Dcx* KO mice

We next questioned the impact of aging on *Dcx* KO behaviors. As expected, all animals gained weight with aging, and we observed no body-weight differences between WT and *Dcx* KO mice (**Supplementary Fig. 5**, all statistical data presented in **Supplementary Table 9**). However, we observed reduced locomotor activity in *Dcx* KO compared to WT mice both in a cyclotron and in open-field tests (**Fig. 6 A,B**). In both tests, locomotion decreased with aging, but was notably already reduced in young *Dcx* KO mice (significant in the cyclotron, but not in the open-field test).

Memory deficits, as tested in the fear conditioning paradigm, were previously reported in adult *Dcx* KO mice on a mixed genetic background (Corbo et al., 2002): following exposure to a CS (auditory cue) paired with a foot shock (US), KO mice froze less compared to WT when re-exposed to the context (contextual memory) or to the CS in a novel context (cued memory). We thus tested our young and mature mice in this paradigm. Both genotypes showed similar acquisition following the conditioning paradigm (**Supplementary Fig. 5**). However, both contextual (24 h after fear conditioning) and cued memory (48 h after fear conditioning) were impaired in *Dcx* KO compared to WT mice (not significant in young but significant in mature), and freezing appeared to decrease with aging in both genotypes, but especially in the KO (**Fig 6 C,D**). Thus, *Dcx* KO mice show impairments in hippocampal-dependent behavior, particularly in mature mice.

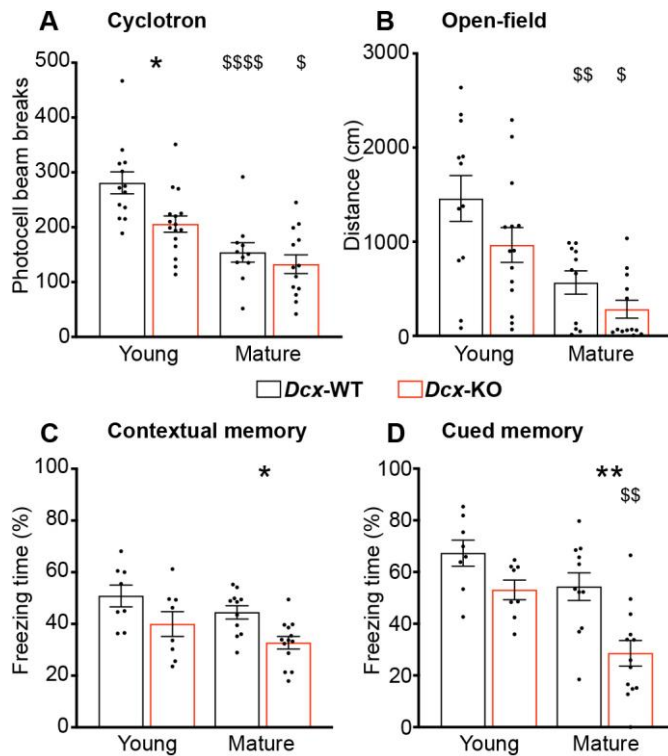


Figure 6. Hypoactivity and impaired contextual and cued memory in *Dcx* KO mice.

Novelty induced-locomotion during 30 min in a cyclotron (A) and during 9 min in the open-field test (B). In both tests, activity differs between genotypes and decreased significantly with age (Cyclotron: ANOVA, Genotype, $F(1, 49) = 7.676$, $p = 0.0079$; Age: $F(1, 49) = 32.89$, $p < 0.0001$; G x A interaction: $F(1, 49) = 2.352$, ns). Open-field, ANOVA: Genotype, $F(1, 46) = 5.047$, $p = 0.0294$; Age: $F(1, 46) = 20.74$, $p < 0.0001$; G x A interaction: $F(1, 46) = 0.3653$, ns). (C) Contextual fear memory recall: 24 h after conditioning, when mice were re-exposed to the aversive context, *Dcx* KO mice froze significantly less than WT but there was not a significant decrease in contextual memory with age (ANOVA: Genotype, $F(1, 36) = 11.28$, $p = 0.0019$; Age: $F(1, 36) = 4.048$, $p = 0.0518$; G x A interaction: $F(1, 36) = 0.01645$, ns). (D) Cued fear memory recall: 24h after the contextual memory recall, when re-exposed to the aversive tone, *Dcx* KO mice froze significantly less than WT and cued memory decreased significantly with age, (ANOVA: Genotype, $F(1, 36) = 14.98$, $p = 0.0004$; Age: $F(1, 36) = 13.16$, $p = 0.0005$; G x A interaction: $F(1, 36) = 1.251$, ns). Values represent means +/- SEM. * vs WT and \$ v. Young, * < 0.05 , ** < 0.01 , **** < 0.0001 .

4. Conclusions

Dcx mutant mice show a hippocampal lamination defect due to perturbed neuronal migration, as well as molecular and ultrastructural changes indicating altered organelle function postnatally (Khalaf-Nazzal et al., 2013; 2017). Here our molecular, ultrastructural, cellular and behavioral studies questioned how the mutation of this developmentally-regulated gene continues to affect organelle function from immature stages to advanced maturation of CA3 neurons. We were interested in testing the contribution of intrinsic organelle defects to hippocampal phenotypes in the adult, which may contribute, together with connectivity defects due to abnormal neuronal position, to altered neuron function

(Deller et al., 1999; Bazelot et al., 2012; D'Amour et al., 2020). Our data show abnormal mitochondrial and GA number, structure and position, persistent even in mature adult neurons. Behavioral tests performed at different ages suggest that whilst younger *Dcx* mutant mice may only be mildly impaired, older mutant mice show clear defects compared to WT littermates, suggesting impaired hippocampal function with aging.

We first used primary cultures of hippocampal neurons to investigate the relationship between previously described morphological abnormalities and organelle characteristics, which we hypothesized were causally related. Changed distribution of these organelles during neuron development has previously been associated with abnormal morphologies and maturation (Horton et al., 2005; López-Doménech et al., 2016; Rangaraju et al., 2019). Although we did find changes related to mitochondria and GA in *Dcx* mutant neurons, we did not observe the expected abnormal neuron morphologies previously described at this developmental stage. Whereas an excess of main process branches was identified in immature *Dcx* KO hippocampal neurons from a mixed genetic background (Bielas et al., 2007), in an additional RNAi study in rat hippocampal neurons, the degree of branching was found to be reduced (Tint et al., 2009). Thus, these previous studies and our results indicate that the species and model used, genetic background, type of mutation, and culture conditions may influence neuron development and phenotypic outcomes *in vitro*. As *Dcx* KO neurons are more certain to show a consistent morphological phenotype in intact tissue in which the mutant CA3 is present as a bilayer (reduced dendritic lengths as described in Bazelot et al., 2012), *in vivo* experiments may be necessary to investigate the causal relationship between mitochondria localization and morphology.

Nonetheless, our cell culture data indicates that the number of mitochondria is reduced in processes and at branch points in immature *Dcx* mutant neurons, and in combination with our transcriptome data, this may indicate that trafficking is impaired in general. Mitochondria must be mobilized in response to metabolic need as well as for mitophagy (Chen and Chan, 2009). Thus, it would be interesting in future studies to investigate mature developmental time points *in vivo* when SPI and SPE neurons show reduced dendritic lengths, and when mitochondrial dynamics show compartment-specific changes in size (Chen and Chan, 2009). On the other hand, mitochondrial anterograde trafficking was not found to be affected in *Dcx* RNAi treated hippocampal neurons in culture (Liu et al., 2012). Other explanations for fewer mitochondria may be altered production or mitophagy. Several upregulated autophagy genes (*Atg2a*, *Atg7*, *Atg16l1*, *Atg5*) were indeed identified in transcriptome data, of which *Atg5* and *7* have already been shown to play a role in mitophagy or mitochondrial quality control (*Genecards* database, <https://www.genecards.org/>).

We also found that GAs appear less compact in immature *Dcx* mutant neurons in culture, with a subtle increase in the size and number of GA fragments, suggesting organizational

changes. We used a *cis*-GA marker for this analysis, however in order to have a better indication of altered GA structure and because vesicular trafficking may be impaired, as indicated by transcriptome data, analysis with a combination of *cis*- and *trans*-GA markers would also be interesting. Of note, standard confocal microscopy may not be sufficient to easily discriminate between compartments, at least in the somatodendritic domain (Zhou et al., 2014; Anton-Fernandez et al., 2015). For *in vivo* investigation of GA structure at a similar developmental time as our culture studies, we used a *trans*-GA marker, and the only structural difference was the surprising finding that the GA invades basal processes significantly more in WT compared to KO neurons. We were additionally surprised to observe a nearly complete lack of GA outposts in the CA3. These unexpected observations could be due to the use of a *trans*-GA marker; however, we noticed that in some experiments in which the electroporation also reached CA1, neurons in this region showed the expected GA invasion of only the apical dendrite with many GA outposts, suggesting that GA organization in the CA3 may be different at this time point. The organizational change we observed still implicates, corroborated by our transcriptome data, trafficking alterations along the GA-to-membrane pathway, which would be interesting to follow up with trafficking assays. Furthermore, analysis *in vivo* at mature stages is also warranted, potentially when GA outposts are found abundantly in CA3 dendrites, where they are known to nucleate MTs and regulate morphology (Ori-McKenney et al., 2012).

In our transcriptomic and ultrastructural analyses, we particularly focused on the two CA3 layers in the adult *Dcx* mutant hippocampus, comparing pyramidal neurons in each layer. Overall, transcriptome differences were fewer at P60 than in our previous study performed at P0 (Khalaf-Nazzal et al., 2017), and differentially regulated genes at P60 were mostly found in the SPI. This first suggests that P0 data contained a proportion of deregulated developmental genes no longer observed at P60. There are two main reasons why more gene deregulation likely occurs in SPI at P60. We previously showed that SPI is enriched with early-born neurons (Khalaf-Nazzal et al., 2017), whereas SPE contains all other neuronal types residing in a relatively normal location, being more similar in composition and structure to WT. A proportion of deregulated genes in SPI are thus likely to be due to the positional difference, and notably this cell layer is embedded in a region with contaminating cell types. For example, *Npy* was upregulated specifically in SPI samples compared to WT and SPE, and *Npy* immunohistochemistry confirmed the increased association of *Npy*+ soma with the SPI layer, indicating the presence of interneurons in this population. It is unclear what consequences this changed cellular environment may have, but it may contribute to nuclear and nucleoli abnormalities seen with ultrastructural analyses that particularly affect SPI. Nonetheless, we have identified deregulated, neuronal-specific genes in SPI that

influence synaptic plasticity, which may contribute to hyperexcitability and serve as targets for intervention by re-expression and or pharmacology.

Despite the differences between SPI and SPE, the enrichment of gene ontologies related to mitochondria, GA and other organelles was noticeable in both layers when searching for the common deregulated gene categories compared to WT, and is reminiscent of defects in neurodegenerative diseases (Wang et al., 2021; Martínez-Menárguez et al., 2019). Since these deregulated genes were not always restricted to one layer or the other, this suggests that some are due to the *Dcx* mutation (intrinsic) and not related to the abnormal neuronal environment. Based on these data, we hence decided at the ultrastructural level to assess organelle structure at two different adult ages. Interestingly GA structural abnormalities, including swollen and disorganized stacks, were detected in both layers at both ages. Such defects can be correlated with the subtle differences revealed by *cis*- and *trans*-GA marker analyses observed *in vitro* and *in vivo* at immature ages. Mitochondrial abnormalities were increased in SPE compared to WT at both ages, increased in SPI in mature samples compared to WT, but were not obvious in young SPI samples. However, there were notably fewer mitochondria detected in young SPI, which might suggest efficient autophagy processes. Notably, these ultrastructural analyses were restricted to somal mitochondria, but together with *in vitro* data focusing only on mitochondria in processes, these data indicate abnormalities throughout the cell.

Further concerning nuclear diameters and nucleoli size, nuclear diameters were more severely affected in SPI (with also both SPE and SPI further showing reduced nucleolar size in mature cells), notably, nuclear shrinkage has been associated with early processes of neurodegeneration in some genetic conditions (Suzuki et al., 2012). On the other hand, inclusions are another indicator of neurodegeneration, and were not significantly increased in KO cells. Ultimately, combining all ultrastructural results, and despite some variability, both layers are clearly abnormal with notable differences in the isolated SPI layer compared to SPE.

Few cortical malformations have been directly associated with organelle defects as we show here; however, the cellular function of some associated genes implies that organelles may also be affected. Cytoplasmic dynein and kinesins show patient mutations (e.g. Poirier et al., 2013), these proteins being known for their roles in transporting organelles and cargos along microtubules (Jaarsma and Hoogenraad, 2015). Thus, genes coding for dynein heavy chain (*DYNC1H1*), dynein regulators *LIS1* and *NDE1*, as well as a dynein adaptor *BICD2*, all show mutations in cortical malformations (Francis and Cappello, 2021), with subtle GA defects identified in some models (Monda and Cheeseman, 2018; Will et al., 2019). Rasika et al., (2018) have also associated GA defects with postnatal-onset microcephaly. *KIF2A* mutations leading to cortical malformations have also recently been linked to changed

interaction with mitochondrial proteins, although mitochondrial localization appeared unaffected in *Kif2a* mutant neurons (Akkaya et al., 2021). The persistence of organelle defects in these developmental pathologies has not yet been assessed and indeed, abnormal organelles in the adult are more often associated with neurodegenerative disorders (e.g. (Wang et al., 2021; Martínez-Menárguez et al., 2019). Defects in mitochondrial transport have in particular been associated with numerous neurodegenerative diseases (Schon and Przedborski, 2011; Misgeld and Schwarz, 2017). However, certain links have recently been proposed between neurodevelopmental abnormalities and possible neurodegeneration (Barnat et al., 2020; Capizzi et al., 2022). In these latter disorders, mitochondria can show fission and fusion defects and GA can show extensive fragmentation. The anomalies we identify in *Dcx* mutants appear different (Knebel-Nazzari et al., 2013 and this paper), since mutant mitochondria have impaired cristae but appear the same size as in WT cells. It should be noted that many normal mitochondria are also present in *Dcx* mutant neurons, and other assays would be required to definitively identify mitophagy and mitochondrial transport defects. Nevertheless, organelle defects in *Dcx* mutant neurons do appear similar to those seen in neurodegenerative conditions, albeit less severe. Together these data suggest long-lasting defects in organelles and other dynamic processes in neurons including trafficking, with potential overlaps in processes known to contribute to neurodegeneration. Thus we sought to further investigate behavioral alterations that may arise in KO mice, particularly as they age.

Using a large battery of tests, we previously reported normal hippocampal-dependent memory in *Dcx* KO young adult mice maintained on the C57Bl/6J genetic background (Germain et al., 2013). However, contextual and cued memory deficits were observed in another *Dcx* KO line either maintained on a mixed (NIH Black Swiss, 129/SvJ) or an inbred 129/SvJ genetic background (Corbo et al., 2002). In the present study, we assessed *Dcx* KO young and mature mice on the 129/SvJ background. After fear conditioning, both context as well as cued memory were impaired in *Dcx* KO mice, particularly in mature animals, whereas WT mice did not greatly worsen with age. The performances of young KO mice also showed tendencies to be lower than either young or mature WT mice. Thus, *Dcx* KO mice appear to reduce their hippocampal memory capacity with age, with tests also implicating other brain regions, e.g. the amygdala. However, the contextual defect confirms the presence of hippocampal deficiencies, especially in mature animals. We also explored hippocampal memory in further tests (paired associate, spatial span, elevated O-maze and object recognition), although difficulties were identified related to the non-performance of mice from this background strain. It is indeed often impossible to study certain phenotypes in inbred genetic backgrounds because the parental strain is already affected. For example, most 129Sv and DBA strains show poor hippocampal dependent learning (Upchurch and Wehner,

1988; Wolfer et al., 1997; “Banbury conference”, 1997). It is not possible at this stage to extrapolate from molecular and cellular to behavioral data; however, we can conclude that defects detected in pyramidal cells are likely to contribute to the memory defects observed.

In conclusion, we identify a neurodevelopmental problem that can permanently affect organelles, revealed in adult *Dcx* KO neurons. Even though *Dcx* is not expressed in mature neurons, cellular defects persist, but are not necessarily worsened across the ages studied. Such structural defects may impact function, perhaps contributing to the previously reported increased cellular excitability in the *Dcx* KO hippocampus (Bazelot et al., 2012); however, in terms of behavior, impairments only become significant in older animals, such as in the hippocampal memory tests reported in this study. It is interesting therefore that neurons may be able to function relatively well, despite a proportion of their organelles being structurally deficient. Although at P60 we detected indications of organelle abnormalities, potentially reminiscent of neurodegeneration, these abnormalities appear to differ or be more subtle, and it seems likely that only older *Dcx* hippocampal neurons show some early signs of this phenomenon. There is hence only moderate evidence of precocious ageing in this model, suggesting that at the behavioral level, older animals may age less well.

Acknowledgements

We thank Sylvie Dumont for initial aid with laser microdissection and G. Martinez-Lorenzana for experimental help with electron microscopy. We thank the animal experimentation facility and cellular and tissue imaging platforms at the Institut du Fer à Moulin, supported also by the Région Ile de France and the FRC Rotary. The Francis lab was associated with the BioPsy Labex project and the Ecole des Neurosciences de Paris Ile-de-France (ENP) network. Our salaries and lab were supported by Inserm, the Centre national de la recherche scientifique (CNRS) and Sorbonne University. The Francis group obtained the following funding contributing to this project: the European Union (EU-HEALTH-2013, DESIRE, N° 60253), the JTC 2015 Neurodevelopmental Disorders affiliated with the French Agence National de la Recherche (for NEURON8-Full- 815-006 STEM-MCD, to FF), E-Rare-3, the ERA-Net for Research on Rare Diseases affiliated with the French ANR (ERARE18-049), the European Cooperation on Science and Technology (COST Action CA16118).

There are no competing interests.

Author contributions

MS: Investigation, Methodology, Analysis, Conceptualization; MNB: Investigation, Methodology, Analysis, Conceptualization, Writing, Supervision; RKN: Investigation,

Methodology, Analysis; GA: Investigation, Methodology; GG: Methodology; EB: Investigation, Methodology; CCD: Investigation, Methodology, Analysis, Writing; VL: Methodology; RO: Investigation, Methodology, Analysis, Conceptualization, Supervision; JFD: Resources, Supervision; FF: Conceptualization, Funding acquisition, Analysis, Data Curation, Resources, Supervision, Validation, Writing, Review and Editing.

References

- Antón-Fernández, A., León-Espinosa, G., DeFelipe, J., Muñoz, A., 2015. Changes in the Golgi Apparatus of Neocortical and Hippocampal Neurons in the Hibernating Hamster. *Front Neuroanat.* 9,157. [https://doi: 10.3389/fnana.2015.00157](https://doi.org/10.3389/fnana.2015.00157)
- Akkaya, C., Atak, D., Kamacioglu, A., Akarlar, B.A., Guner, G., Dayam, E., Taskin, A.C., Ozlu, N., Ince-Dunn, G., 2021. Roles of developmentally regulated KIF2A alternative isoforms in cortical neuron migration and differentiation. *Development* 148, dev192674. <https://doi.org/10.1242/dev.192674>
- Bahi-Buisson, N., Souville, I., Fourniol, F.J., Toussaint, A., Moores, C.A., Houdusse, A., Yves Lemaitre, J., Poirier, K., Khalaf-Nazzal, R., Hully, M., Louis Leger, P., Elie, C., Boddaert, N., Beldjord, C., Chelly, J., Francis, F., SBH-LIS European Consortium, 2013. New insights into genotype-phenotype correlations for the doublecortin-related lissencephaly spectrum. *Brain* 136, 223–244. <https://doi.org/10.1093/brain/aws323>
- Barnat, M., Capizzi, M., Aparicio, E., Deluda, S., Wennagel, D., Kacher, R., Kassem, R., Lenoir, S., Agasse, F., Braz, B., Liu, J.P., Ighil, J., Tessier, A., Zeitlin, S.O., Duyckaerts, C., Dommergues, M., Durr, A., Humbert, S., 2020. Huntington's disease alters human neurodevelopment. *Science*. 369(6505), 787-793. [https://doi: 10.1126/science.aax3303](https://doi.org/10.1126/science.aax3303)
- Bazelot, M., Simonnet, J., Dinocourt, C., Bruel-Jungerman, E., Miles, R., Fricker, D., Francis, F., 2012. Cellular anatomy, physiology and epileptiform activity in the CA3 region of *Dcx* knockout mice: a neuronal lamination defect and its consequences. *Eur. J. Neurosci.* 35, 244–256. <https://doi.org/10.1111/j.1460-9568.2011.07962.x>
- Belvindrah, R., Nosten-Bertrand, M., Francis, F., 2014. Neuronal migration and its disorders affecting the CA3 region. *Front Cell Neurosci* 8, 63. <https://doi.org/10.3389/fncel.2014.00063>
- Bielas, S.L., Serneo, F.F., Chechlacz, M., Deerinck, T.J., Perkins, G.A., Allen, P.B., Ellisman, M.H., Gleeson, J.G., 2007. Spinophilin Facilitates Dephosphorylation of Doublecortin by PP1 to Mediate Microtubule Bundling at the Axonal Wrist. *Cell* 129, 579–591. <https://doi.org/10.1016/j.cell.2007.03.023>
- Bustin, S.A., Benes, V., Garson, J.A., Hellems, J., Huggett, J., Kubista, M., Mueller, R., Nolan, T., Pfaffl, M.W., Shipley, G.L., Vandesompele, J., Wittwer, C.T., 2009. The

- MIQE Guidelines: Minimum Information for Publication of Quantitative Real-Time PCR Experiments. *Clinical Chemistry* 55, 611–622.
<https://doi.org/10.1373/clinchem.2008.112797>
- Capizzi, M., Carpentier, R., Denarier, E., Adrait, A., Kassem, R., Mapelli, M., Couté, Y., Humbert, S., 2022. Developmental defects in Huntington's disease show that axonal growth and microtubule reorganization require NUMA1. *Neuron*. 110(1), 36-50.e5.
<https://doi: 10.1016/j.neuron.2021.10.033>
- Chen, H., Chan, D.C., 2009. Mitochondrial dynamics--fusion, fission, movement, and mitophagy--in neurodegenerative diseases. *Hum Mol Genet*. 18(R2):R169-76.
<https://doi: 10.1093/hmg/ddp326>
- Chiu, S.L., Diering, G.H., Ye, B., Takamiya, K., Chen, C.M., Jiang, Y., Niranjan, T., Schwartz, C.E., Wang, T., Huganir, R.L., 2017. GRASP1 Regulates Synaptic Plasticity and Learning through Endosomal Recycling of AMPA Receptors. *Neuron*. 93(6), 1405-1419.e8. <https://doi: 10.1016/j.neuron.2017.02.031>
- Corbo, J.C., Deuel, T.A., Long, J.M., LaPorte, P., Tsai, E., Wynshaw-Boris, A., Walsh, C.A., 2002. Doublecortin Is Required in Mice for Lamination of the Hippocampus But Not the Neocortex. *J. Neurosci*. 22, 7548–7557. <https://doi.org/10.1523/JNEUROSCI.22-17-07548.2002>
- D'Amour, J.A., Ekins, T., Ganatra, S., Yuan, X., McBain, C.J., 2020. Aberrant sorting of hippocampal complex pyramidal cells in type I lissencephaly alters topological innervation. *Elife* 9, e55173. <https://doi.org/10.7554/eLife.55173>
- Delahaye-Duriez, A., Srivastava, P., Chkura, K. et al. 2016. Rare and common epilepsies converge on a shared gene regulatory network providing opportunities for novel antiepileptic drug discovery. *Genome Biol* 17, 245 (2016).
<https://doi.org/10.1186/s13059-016-1097-7>
- Deller, T., Drakew, A., Heimrich, B., Förster, E., Tielsch, A., Frotscher, M., 1999. The hippocampus of the reeler mutant mouse: fiber segregation in area CA1 depends on the position of the postsynaptic target cells. *Exp Neurol* 156, 254–267.
<https://doi.org/10.1006/exnr.1999.7021>
- Dennis, G., Sherman, B.T., Hosack, D.A., Yang, J., Gao, W., Lane, H.C., Lempicki, R.A., 2003. DAVID: Database for Annotation, Visualization, and Integrated Discovery. *Genome Biol* 4, P3.
- des Portes, V., Pinard, J.M., Billuart, P., Vinet, M.C., Koulakoff, A., Carrié, A., Gelot, A., Dupuis, E., Motte, J., Berwald-Netter, Y., Catala, M., Kahn, A., Beldjord, C., Chelly, J., 1998. A novel CNS gene required for neuronal migration and involved in X-linked subcortical laminar heterotopia and lissencephaly syndrome. *Cell*. 92(1), 51-61.
[https://doi: 10.1016/s0092-8674\(00\)80898-3](https://doi: 10.1016/s0092-8674(00)80898-3)

- Di Donato N, Di Donato, N., Timms, A.E., Aldinger, K.A., Mirzaa, G.M., Bennett, J.T., Collins, S., Olds, C., Mei, D., Chiari, S., Carvill, G., Myers, C.T., Rivière, J.-B., Zaki, M.S., Gleeson, J.G., Rump, A., Conti, V., Parrini, E., Ross, M.E., Ledbetter, D.H., Guerrini, R., Dobyns, W.B., 2018. Analysis of 17 genes detects mutations in 81% of 811 patients with lissencephaly. *Genet Med* 20, 1354–1364. <https://doi.org/10.1038/gim.2018.8>
- Faits, M.C., Zhang, C., Soto, F., Kerschensteiner, D., 2016. Dendritic mitochondria reach stable positions during circuit development. *eLife* 5, e11583. <https://doi.org/10.7554/eLife.11583>
- Francis, F., Cappello, S., 2021. Neuronal migration and disorders – an update. *Current Opinion in Neurobiology* 66, 57–68. <https://doi.org/10.1016/j.conb.2020.10.002>
- Francis, F., Koulakoff, A., Boucher, D., Chafey, P., Schaar, B., Villet, M.-C., Friocourt, G., McDonnell, N., Reiner, O., Kahn, A., McConnell, S.K., Berwald-Netter, Y., Denoulet, P., Chelly, J., 1999. Doublecortin Is a Developmentally Regulated, Microtubule-Associated Protein Expressed in Migrating and Differentiating Neurons. *Neuron* 23, 247–256. [https://doi.org/10.1016/S0896-6273\(00\)80777-1](https://doi.org/10.1016/S0896-6273(00)80777-1)
- Germain, J., Bruel-Jungerman, E., Grannec, C., Ferris, C., Lepousez, G., Giros, B., Francis, F., Nosten-Bertrand, M., 2013. Doublecortin knockout mice show normal hippocampal-dependent memory despite CA3 lamination defects. *PLoS ONE* 8, e74992. <https://doi.org/10.1371/journal.pone.0074992>
- Gleeson, J.G., Allen, K.M., Fox, J.W., Lanperti, E.D., Berkovic, S., Scheffer, I., Cooper, E.C., Dobyns, W.B., Minnerath, S.K., Ross, M.E., Walsh, C.A., 1998. doublecortin, a Brain-Specific Gene Mutated in Human X-Linked Lissencephaly and Double Cortex Syndrome, Encodes a Putative Signaling Protein. *Cell* 92, 63–72. [https://doi.org/10.1016/S0092-8674\(00\)80899-5](https://doi.org/10.1016/S0092-8674(00)80899-5)
- Gleeson, J.G., Lin, P.T., Flanagan, L.A., Walsh, C.A., 1999. Doublecortin Is a Microtubule-Associated Protein and Is Expressed Widely by Migrating Neurons. *Neuron* 23, 257–271. [https://doi.org/10.1016/S0896-6273\(00\)80778-3](https://doi.org/10.1016/S0896-6273(00)80778-3)
- Hell, J.W., 2014. CaMKII: claiming center stage in postsynaptic function and organization. *Neuron*. 81(2), 249-65. <https://doi.org/10.1016/j.neuron.2013.12.024>.
- Horton, A.C., Rácz, B., Monson, E.E., Lin, A.L., Weinberg, R.J., Ehlers, M.D., 2005. Polarized secretory trafficking directs cargo for asymmetric dendrite growth and morphogenesis. *Neuron* 48, 757–771. <https://doi.org/10.1016/j.neuron.2005.11.005>
- Jaarsma, D., Hoogenraad, C.C., 2015. Cytoplasmic dynein and its regulatory proteins in Golgi pathology in nervous system disorders. *Front Neurosci* 9, 397. <https://doi.org/10.3389/fnins.2015.00397>

- Jia, Z., Agopyan, N., Miu, P., Xiong, Z., Henderson, J., Gerlai, R., Taverna, F.A., Velumian, A., MacDonald, J., Carlen, P., Abramow-Newerly, W., Roder, J., 1996. Enhanced LTP in mice deficient in the AMPA receptor GluR2. *Neuron*. 17(5), 945-56. [https://doi: 10.1016/s0896-6273\(00\)80225-1](https://doi.org/10.1016/s0896-6273(00)80225-1).
- Kappeler, C., Saillour, Y., Baudoin, J.-P., Tuy, F.P.D., Alvarez, C., Houbron, C., Gaspar, P., Hamard, G., Chelly, J., Métin, C., Francis, F., 2006. Branching and nucleokinesis defects in migrating interneurons derived from doublecortin knockout mice. *Human Molecular Genetics* 15, 1387–1400. <https://doi.org/10.1093/hmg/ddl062>
- Keller, J.N., Dimayuga, E., Chen, Q., Thorpe, J., Gee, J., Ding, Q., 2004. Autophagy, proteasomes, lipofuscin, and oxidative stress in the aging brain. *Int J Biochem Cell Biol.* 36(12), 2376-91. [https://doi: 10.1016/j.biocel.2004.03.003](https://doi.org/10.1016/j.biocel.2004.03.003)
- Khalaf-Nazzal, R., Bruel-Jungerman, E., Rio, J.-P., Bureau, J., Iriopoulou, T., Sumia, I., Roumegous, A., Martin, E., Olaso, R., Parras, C., Cifuentes-Diaz, C., Francis, F., 2013. Organelle and Cellular Abnormalities Associated with Hippocampal Heterotopia in Neonatal Doublecortin Knockout Mice. *PLoS ONE* 8, e72622. <https://doi.org/10.1371/journal.pone.0072622>
- Khalaf-Nazzal, R., Stouffer, M.A., Olaso, R., Mounssan, L., Roumegous, A., Lavilla, V., Carpentier, W., Moutkine, I., Dumont, S., Albaud, B., Cagnard, N., Roest Crollius, H., Francis, F., 2017. Early born neurons are abnormally positioned in the doublecortin knockout hippocampus. *Hum. Mol. Genet.* 26, 90–108. <https://doi.org/10.1093/hmg/ddw070>
- Kimura, T., Murakami, F., 2014. Evidence That Dendritic Mitochondria Negatively Regulate Dendritic Branching in Pyramidal Neurons in the Neocortex. *Journal of Neuroscience* 34, 6938–6951. <https://doi.org/10.1523/JNEUROSCI.5095-13.2014>
- Koizumi, H., Higginbotham, M., Poon, T., Tanaka, T., Brinkman, B.C., Gleeson, J.G., 2006. Doublecortin maintains bipolar shape and nuclear translocation during migration in the adult forebrain. *Nat Neurosci* 9, 779–786. <https://doi.org/10.1038/nn1704>
- Küry S., van Woerden, G.M., Besnard, T., Proietti Onori, M., Latypova, X., Towne, M.C., Cho, M.T., Prescott, T.E., Ploeg, M.A., Sanders, S., Stessman, H.A.F., Pujol, A., Distel, B., Robak, L.A., Bernstein, J.A., Denommé-Pichon, A.S., Lesca, G., Sellars, E.A., Berg, J., Carré, W., Busk, Ø.L., van Bon, B.W.M., Waugh, J.L., Deardorff, M., Hoganson, G.E., Bosanko, K.B., Johnson, D.S., Dabir, T., Holla, Ø.L., Sarkar, A., Tveten, K., de Bellecize, J., Braathen, G.J., Terhal, P.A., Grange, D.K., van Haeringen, A., Lam, C., Mirzaa, G., Burton, J., Bhoj, E.J., Douglas, J., Santani, A.B., Nesbitt, A.I., Helbig, K.L., Andrews, M.V., Begtrup, A., Tang, S., van Gassen, K.L.I., Juusola, J., Foss, K., Enns, G.M., Moog, U., Hinderhofer, K., Paramasivam, N., Lincoln, S., Kusako, B.H., Lindenbaum, P., Charpentier, E., Nowak, C.B., Cherot, E.,

- Simonet, T., Ruivenkamp, C.A.L., Hahn, S., Brownstein, C.A., Xia, F., Schmitt, S., Deb, W., Bonneau, D., Nizon, M., Quinquis, D., Chelly, J., Rudolf, G., Sanlaville, D., Parent, P., Gilbert-Dussardier, B., Toutain, A., Sutton, V.R., Thies, J., Peart-Vissers, L.E.L.M., Boisseau, P., Vincent, M., Grabrucker, A.M., Dubourg, C.; Undiagnosed Diseases Network, Tan, W.H., Verbeek, N.E., Granzow, M., Santen, G.W.E., Shendure, J., Isidor, B., Pasquier, L., Redon, R., Yang, Y., State, M.W., Kleefstra, T., Cogné, B.; GEM HUGO; Deciphering Developmental Disorders Study, Petrovski, S., Retterer, K., Eichler, E.E., Rosenfeld, J.A., Agrawal, P.B., Bézieau, S., Odent, S., Elgersma, Y., Mercier, S., 2017. De Novo Mutations in Protein Kinase Genes CAMK2A and CAMK2B Cause Intellectual Disability. *Am J Hum Genet.* 101(5), 768-788. <https://doi.org/10.1016/j.ajhg.2017.10.003>
- Lasser, M., Tiber, J., Lowery, L.A., 2018. The Role of the Microtubule Cytoskeleton in Neurodevelopmental Disorders. *Front. Cell. Neurosci.* 12, 165. <https://doi.org/10.3389/fncel.2018.00165>
- Liu, J.S., Schubert, C.R., Fu, X., Fourniol, F.J., Jaiswal, J.K., Houdusse, A., Stultz, C.M., Moores, C.A., Walsh, C.A., 2012. Molecular Basis for Specific Regulation of Neuronal Kinesin-3 Motors by Doublecortin Family Proteins. *Molecular Cell* 47, 707–721. <https://doi.org/10.1016/j.molcel.2012.06.025>
- Livak, K.J., Schmittgen, T.D., 2001. Analysis of Relative Gene Expression Data Using Real-Time Quantitative PCR and the $2^{-\Delta\Delta CT}$ Method. *Methods* 25, 402–408. <https://doi.org/10.1006/meth.2001.1262>
- López-Doménech, G., Higgs, N.F., Vaccaro, V., Roš, H., Arancibia-Cárcamo, I.L., MacAskill, A.F., Kittler, J.T., 2016. Loss of Dendritic Complexity Precedes Neurodegeneration in a Mouse Model with Disrupted Mitochondrial Distribution in Mature Dendrites. *Cell Reports* 17, 317–327. <https://doi.org/10.1016/j.celrep.2016.09.004>
- Maes, M.E., Schlamp, C., Nickells, R.W., 2017. Live-cell imaging to measure BAX recruitment kinetics to mitochondria during apoptosis. *PLoS One.* 12(9), e0184434. <https://doi.org/10.1371/journal.pone>
- Manka, S.W., Moores, C.A., 2020. Pseudo-repeats in doublecortin make distinct mechanistic contributions to microtubule regulation. *EMBO Rep* 21. <https://doi.org/10.15252/embr.202051534>
- Martínez-Menárguez, J.Á., Tomás, M., Martínez-Martínez, N., Martínez-Alonso, E., 2019. Golgi Fragmentation in Neurodegenerative Diseases: Is There a Common Cause? *Cells* 8, E748. <https://doi.org/10.3390/cells8070748>
- Misgeld, T., Schwarz, T.L., 2017. Mitostasis in Neurons: Maintaining Mitochondria in an Extended Cellular Architecture. *Neuron* 96, 651–666. <https://doi.org/10.1016/j.neuron.2017.09.055>

- Monda, J.K., Cheeseman, I.M., 2018. Nde1 promotes diverse dynein functions through differential interactions and exhibits an isoform-specific proteasome association. *Mol Biol Cell* 29, 2336–2345. <https://doi.org/10.1091/mbc.E18-07-0418>
- Mutant mice and neuroscience: recommendations concerning genetic background. Banbury Conference on genetic background in mice, 1997. . *Neuron* 19, 755–759. [https://doi.org/10.1016/s0896-6273\(00\)80958-7](https://doi.org/10.1016/s0896-6273(00)80958-7)
- Nosten-Bertrand, M., Kappeler, C., Dinocourt, C., Denis, C., Germain, J., Phan Dinh Tuy, F., Verstraeten, S., Alvarez, C., Métin, C., Chelly, J., Giros, B., Miles, R., Depaulis, A., Francis, F., 2008. Epilepsy in *Dcx* knockout mice associated with discrete lamination defects and enhanced excitability in the hippocampus. *PLoS ONE* 3, e2473. <https://doi.org/10.1371/journal.pone.0002473>
- Ori-McKenney, K.M., Jan, L.Y., Jan, Y.N., 2012. Golgi outposts shape dendrite morphology by functioning as sites of acentrosomal microtubule nucleation in neurons. *Neuron* 76(5), 921-30. <https://doi.org/10.1016/j.neuron.2012.10.008>.
- Penzo, M.A., Robert, V., Tucciarone, J., De Bundel, D., Wang, M., Van Aelst, L., Darvas, M., Parada, L.F., Palmiter, R.D., He, M., Huang, Z.J., Li, B., 2015. The paraventricular thalamus controls a central amygdala fear circuit. *Nature* 519, 455–459. <https://doi.org/10.1038/nature13978>
- Poirier, K., Lebrun, N., Broix, L., Tian, G., Chaillour, Y., Boscheron, C., Parrini, E., Valence, S., Pierre, B.S., Oger, M., Lacombe, D., Geneviève, D., Fontana, E., Darra, F., Cances, C., Barth, M., Bonneau, D., Leandina, B.D., N'guyen, S., Gitiaux, C., Parent, P., des Portes, V., Pedespan, J.M., Legrez, V., Castelnau-Ptakine, L., Nitschke, P., Hieu, T., Masson, C., Zelenika, D., Andrieux, A., Francis, F., Guerrini, R., Cowan, N.J., Bahi-Buisson, N., Chelly, J., 2013. Mutations in *TUBG1*, *DYNC1H1*, *KIF5C* and *KIF2A* cause malformations of cortical development and microcephaly. *Nat Genet* 45, 639–647. <https://doi.org/10.1038/ng.2613>
- Rangaraju, V., Lewis, T.L., Hirabayashi, Y., Bergami, M., Motori, E., Cartoni, R., Kwon, S.-K., Courchet, J., 2019. Pleiotropic Mitochondria: The Influence of Mitochondria on Neuronal Development and Disease. *J Neurosci* 39, 8200–8208. <https://doi.org/10.1523/JNEUROSCI.1157-19.2019>
- Rasika, S., Passemard, S., Verloes, A., Gressens, P., El Ghouzzi, V., 2018. Golgipathies in Neurodevelopment: A New View of Old Defects. *Dev Neurosci* 40, 396–416. <https://doi.org/10.1159/000497035>
- Raux, G., Bumsel, E., Hecketsweiler, B., van Amelsvoort, T., Zinkstok, J., Manouvrier-Hanu, S., Fantini, C., Brévière, G.M., Di Rosa, G., Pustorino, G., Vogels, A., Swillen, A., Legallic, S., Bou, J., Opolczynski, G., Drouin-Garraud, V., Lemarchand, M., Philip, N., Gérard-Desplanches, A., Carlier, M., Philippe, A., Nolen, M.C., Heron, D., Sarda, P.,

- Lacombe, D., Coizet, C., Alembik, Y., Layet, V., Afenjar, A., Hannequin, D., Demily, C., Petit, M., Thibaut, F., Frebourg, T., Campion, D., 2007. Involvement of hyperprolinemia in cognitive and psychiatric features of the 22q11 deletion syndrome. *Hum Mol Genet.* 16(1), 83-91. [https://doi: 10.1093/hmg/ddl443](https://doi.org/10.1093/hmg/ddl443).
- Romero, D.M., Bahi-Buisson, N., Francis, F., 2018. Genetics and mechanisms leading to human cortical malformations. *Seminars in Cell & Developmental Biology* 76, 33–75. <https://doi.org/10.1016/j.semcdb.2017.09.031>
- Salpietro, V., Dixon, C.L., Guo, H., Bello, O.D., Vandrovicova, J., Efthymiou, S., Maroofian, R., Heimer, G., Burglen, L., Valence, S., Torti, E., Hacke, M., Rankin, J., Tariq, H., Colin, E., Procaccio, V., Striano, P., Mankad, K., Lieb, A., Chen, S., Pisani, L., Bettencourt, C., Männikkö, R., Manole, A., Brusco, A., Grasso, E., Ferrero, G.B., Armstrong-Moron, J., Gueden, S., Bar-Yosef, O., Tza'ok, M., Monaghan, K.G., Santiago-Sim, T., Person, R.E., Cho, M.T., Willaer, R., Yoo, Y., Chae, J.H., Quan, Y., Wu, H., Wang, T., Bernier, R.A., Xia, K., Blesson, A., Jain, M., Motazacker, M.M., Jaeger, B., Schneider, A.L., Boysen, K., Mui, A.M., Myers, C.T., Gavrilova, R.H., Gunderson, L., Schultz-Rogers, L., Klee, F.V., Dymont, D., Osmond, M., Parellada, M., Llorente, C., Gonzalez-Peñas, J., Carracedo, A., Van Haeringen, A., Ruivenkamp, C., Nava, C., Heron, D., Nardello, R., Iacolino, M., Minetti, C., Skabar, A., Fabretto, A.; SYNAPS Study Group, Raspall-Chaure, M., Chez, M., Tsai, A., Fassi, E., Shinawi, M., Constantino, J.N., De Zorzi, P., Fortuna, S., Kok, F., Keren, B., Bonneau, D., Choi, M., Benzeev, B., Zara, F., Mefford H.C., Scheffer, I.E., Clayton-Smith, J., Macaya, A., Rothman, J.F., Eichler, E.E., Kullmann, D.M., Houlden, H., 2019 AMPA receptor GluA2 subunit defects are a cause of neurodevelopmental disorders. *Nat Commun.* 10(1), 3004. [https://doi: 10.1038/s41467-019-10910-w](https://doi.org/10.1038/s41467-019-10910-w)
- Sapir, T., 2000. Double cysteine mutations cluster in evolutionarily conserved functional domains. *Human Molecular Genetics* 9, 703–712. <https://doi.org/10.1093/hmg/9.5.703>
- Schon, E.A., Przedborski, S., 2011. Mitochondria: the next (neurode)generation. *Neuron* 70, 1033–1053. <https://doi.org/10.1016/j.neuron.2011.06.003>
- Schulz, D., Morschel, J., Schuster, S., Eulenburg, V., Gomeza, J., 2018. Inactivation of the Mouse L-Proline Transporter PROT Alters Glutamatergic Synapse Biochemistry and Perturbs Behaviors Required to Respond to Environmental Changes. *Front Mol Neurosci.* 11, 279. [https://doi: 10.3389/fnmol.2018.00279](https://doi.org/10.3389/fnmol.2018.00279).
- Stouffer, M.A., Golden, J.A., Francis, F., 2016. Neuronal migration disorders: Focus on the cytoskeleton and epilepsy. *Neurobiol. Dis.* 92, 18–45. <https://doi.org/10.1016/j.nbd.2015.08.003>

- Suzuki, Y., Yamazaki, Y., Hozumi, Y., Okada, M., Tanaka, T., Iseki, K., Ohta, N., Aoyagi, M., Fujii, S., Goto, K., 2012. NMDA receptor-mediated Ca(2+) influx triggers nucleocytoplasmic translocation of diacylglycerol kinase ζ under oxygen-glucose deprivation conditions, an in vitro model of ischemia, in rat hippocampal slices. *Histochem Cell Biol* 137, 499–511. <https://doi.org/10.1007/s00418-011-0907-y>
- Tasic, B., Menon, V., Nguyen, T.N., Kim, T.K., Jarsky, T., Yao, Z., Levi, B., Gray, L.T., Sorensen, S.A., Dolbeare, T., Bertagnolli, D., Goldy, J., Shapovalova, N., Parry, S., Lee, C., Smith, K., Bernard, A., Madisen, L., Sunkin, S.M., Hawrylycz, M., Koch, C., Zeng, H., 2016. Adult mouse cortical cell taxonomy revealed by single cell transcriptomics. *Nat Neurosci* 19, 335–346. <https://doi.org/10.1038/nn.4216>
- Thayer, D.A., Jan, Y.N., Jan, L.Y., 2013. Increased neuronal activity fragments the Golgi complex. *Proc Natl Acad Sci U S A*. 110(4), 1482-7. <https://doi.org/10.1073/pnas.1220978110>
- Tint, I., Jean, D., Baas, P.W., Black, M.M., 2009. Doublecortin Associates with Microtubules Preferentially in Regions of the Axon Displaying Actin-Rich Protrusive Structures. *Journal of Neuroscience* 29, 10995–11010. <https://doi.org/10.1523/JNEUROSCI.3392-09.2009>
- Upchurch, M., Wehner, J.M., 1988. Differences between inbred strains of mice in Morris water maze performance. *Behav Genet* 18, 55–68. <https://doi.org/10.1007/BF01067075>
- Wang, B., Huang, M., Shang, D., Yan, X., Zhao, B., Zhang, X., 2021. Mitochondrial Behavior in Axon Degeneration and Regeneration. *Front Aging Neurosci* 13, 650038. <https://doi.org/10.3389/fnagi.2021.650038>
- Will, L., Portegies, S., van Scheel, J., van Luyk, M., Jaarsma, D., Hoogenraad, C.C., 2019. Dynein activating adaptor BICD2 controls radial migration of upper-layer cortical neurons in vivo. *Acta Neuropathol Commun* 7, 162. <https://doi.org/10.1186/s40478-019-0827-y>
- Wille, A., Maurer, V., Piatti, P., Whittle, N., Rieder, D., Singewald, N., Lusser, A., 2015. Impaired Contextual Fear Extinction Learning is Associated with Aberrant Regulation of CHD-Type Chromatin Remodeling Factors. *Front. Behav. Neurosci.* 9. <https://doi.org/10.3389/fnbeh.2015.00313>
- Wolfer, D.P., Müller, U., Stagiar, M., Lipp, H.P., 1997. Assessing the effects of the 129/Sv genetic background on swimming navigation learning in transgenic mutants: a study using mice with a modified beta-amyloid precursor protein gene. *Brain Res* 771, 1–13. [https://doi.org/10.1016/s0006-8993\(97\)00673-2](https://doi.org/10.1016/s0006-8993(97)00673-2)

Zhou, W., Chang, J., Wang, X., Savelieff, M.G., Zhao, Y., Ke, S., Ye, B., 2014. GM130 is required for compartmental organization of dendritic golgi outposts. *Curr Biol* 24(11), 1227-33. [https://doi: 10.1016/j.cub.2014.04.008](https://doi.org/10.1016/j.cub.2014.04.008)

Journal Pre-proof

Figure legends

Figure 1. Decreased mitochondria and altered distribution in *Dcx* KO primary hippocampal neurons. (A) WT (left) and KO (right) primary hippocampal neurons at DIV3 labeled with Tuj1 (microtubules, red), mitotracker (green) showing mitochondria located in neuronal processes (asterisk *) and at branch points (arrowheads). Scale bar = 10 μ M. (B) The total number of mitochondria in all processes per cell was significantly decreased in KO neurons compared to WT (Student *t*-test: $t(356) = 2,193$, $p = 0.029$). (C) The decreased number of mitochondria in KO neurons was observed both in main and somal processes: the main process is defined as the longest neurite and somal processes are all other neurites originating from the soma, as described previously (Bielas et al., 2007). (ANOVA: Genotype: $F(1, 354) = 6.27$, $p < 0,0127$; Position: $F(1, 354) = 109.3$, $p < 0.0001$; G x P interaction: ns, $p = 0.6$). (D) The percent of branch points exhibiting mitochondria was significantly decreased in KO neurons compared to WT ($t(241) = 2.305$, $p = 0.022$ test). (E) Size of mitochondria (μ m) located in neuronal processes is not different between genotypes ($t(169) = 0.7127$, ns). N = 85-92 neurons from 8-9 embryos from 4 cultures per genotype. * < 0.05 .

Figure 2. Altered Golgi apparatus size and shape in *Dcx* KO hippocampal neurons. (A) WT (left) and KO (right) primary hippocampal neurons at DIV9 labeled with Tuj1 (microtubules, red), GM130 (GA, green), and DAPI. Scale bar = 10 μ M. (B) GA volume was greater in *Dcx* KO neurons at DIV9 compared to WT (**** $p < 0.0001$; *t* test, $n = 105-114$ neurons from 5-6 embryos from 3 cultures per genotype). (C) There was an increased proportion of *Dcx* KO neurons at DIV9 with ≥ 10 GA fragments (* $p = 0.0238$, χ^2). (D) WT (left) and KO (right) hippocampal neurons at P7-8, which were labeled by *in utero* electroporation at E13.5-14.5 with pCAG-GalT-GFP (GA, green) and pCAG-Tdtomato (cytoplasmic, red). Arrows and asterisks indicate apical and basal processes that contain GA, respectively. Scale bar = 10 μ M. (E) Distribution of GA into apical processes was quantified with no differences detected between the genotypes (χ^2 , distinguishing number of processes 1,2 and 3, apical ns, $n = 66$ WT, 33 KO neurons from 3 litters with 5 WT and 3 KO mice). (F) The longest length of the GA protrusion into apical processes was not altered in *Dcx* KO neurons (Student *t*-test ns). (G) Distribution of GA into basal processes was quantified, and there was a significantly greater proportion of basal processes containing GA in WT CA3 neurons (χ^2 distinguishing number of processes ≥ 2 , basal * $p = 0.0351$, $n = 66$ WT, 33 KO neurons from 3 litters with 5 WT and 3 KO mice).

Figure 3. Dysregulated genes in SPI and SPE corresponding to organelle gene ontologies (A) Laser capture microdissection from cresyl violet stained P60 brain sections. Hippocampal CA3 WT (top) and *Dcx* KO (bottom) internal (SPI) and external (SPE) layers are shown with schematized indications of areas selected for excision (scale bar 300 μ m). **(B)** Venn diagrams showing the number of transcripts up- or downregulated in *Dcx* KO SPI and/or SPE CA3 hippocampal pyramidal cell layers compared to WT (genes with $p < 0.01$, ratio >1.1). DAVID functional clustering of SPI versus WT up- **(C)** and down-regulated **(D)** gene expression differences (transcripts with $p < 0.01$). Each significant functional category (y-axis), is plotted against the value of enrichment score (x-axis).

Figure 4. Altered mitochondria and Golgi apparatus in *Dcx* KO CA3 neurons.

(A,B) High magnification electron micrographs of hippocampal CA3 pyramidal neurons illustrating normal **(A)** or altered **(B, white asterisk)** mitochondria in WT and *Dcx* KO mice respectively. **(C)** Quantitative analyses showing that altered mitochondria (% per cell) significantly differ between CA3 layers and their percentage increased with aging, but differently according to the layers (ANOVA: CA3 Layer, $F(2, 312) = 50.97$, $p < 0.0001$; Age: $F(1, 312) = 39.68$, $p < 0.0001$; L x A interaction: $F(2, 312) = 11.63$, $P < 0.0001$). **(D,E)** High magnification EM of hippocampal CA3 pyramidal neurons illustrating normal **(D)** or altered **(E)** Golgi apparatus in WT and *Dcx* KO mice respectively. **(F)** Both SPE and SPI KO CA3 layers exhibited more altered GA compared with WT, but GA alteration did not worsen with age (ANOVA: CA3 Layers, $F(2, 293) = 37.42$, $p < 0.0001$; Age: $F(1, 293) = 1.056$, ns; L x A interaction: $F(2, 293) = 0.2449$, ns. Values represent means \pm SEM. Scale bars: A,B,D,E, 0.5 μ m. * vs WT, # vs SPE and \$ vs Young. *** < 0.001 , **** < 0.0001 .

Figure 5. Reduced nuclear diameter of hippocampal CA3 pyramidal neurons with aging is more severe in *Dcx* KO SPI layer.

(A-C) Low magnification electron micrographs of hippocampal CA3 pyramidal neurons illustrating nuclear diameter in WT **(A)**, KO-SPE **(B)** and KO-SPI **(C)** layers. **(D)** Nuclear diameter significantly differed between CA3 layers and decreased significantly with age, but in interaction with CA3 layers (ANOVA: CA3 Layers, $F(2, 728) = 52.3$, $P < 0.0001$; Age: $F(1, 728) = 10.95$, $p = 0.001$; L x A interaction: $F(2, 728) = 7.342$, $p < 0.0007$). At both ages, SPI exhibited smaller nuclei compared to WT and SPE layers. No decrease in nuclear diameter with age was observed in WT, and the decrease was more pronounced for SPI compared to the SPE layer. **(E-F)** High magnification electron micrographs of hippocampus CA3 pyramidal neuron illustrating lipofuscin inclusions **(E,F)** and lipofuscin inclusions containing clear areas resembling lipid droplets **(G)**. **(H)** The number of inclusions increased with age (ANOVA: Age: $F(1, 279) = 34.96$, $p < 0.0001$), with a limited effect of the CA3 region (SPI or SPE) to the significance (ANOVA: CA3 Layer: $F(2, 279) = 2.5$, $p = 0.0839$; L x A interaction:

ns): in young adults the SPE layer tended to have more inclusions and in mature, both SPE and SPI layers tended to have more inclusions compared to the WT layer. Values represent means +/- SEM. * vs WT, # vs SPE and \$ vs Young. * < 0.05, ** < 0.01, *** < 0.001, **** < 0.0001.

Figure 6. Hypoactivity and impaired contextual and cued memory in *Dcx* KO mice.

Novelty induced-locomotion during 30 min in a cyclotron (**A**) and during 9 min in the open-field test (**B**). In both tests, activity differs between genotypes and decreased significantly with age (Cyclotron: ANOVA, Genotype, $F(1, 49) = 7.676$, $p = 0.0079$; Age: $F(1, 49) = 32.89$, $p < 0.0001$; G x A interaction: $F(1, 49) = 2.352$, ns). Open-field, ANOVA: Genotype, $F(1, 46) = 5.047$, $p = 0.0294$; Age: $F(1, 46) = 20.74$, $p < 0.0001$; G x A interaction: $F(1, 46) = 0.3653$, ns). (**C**) Contextual fear memory recall: 24 h after conditioning, when mice were re-exposed to the aversive context, *Dcx* KO mice froze significantly less than WT but there was not a significant decrease in contextual memory with age (ANOVA: Genotype, $F(1, 36) = 11.28$, $p = 0.0019$; Age: $F(1, 36) = 4.048$, $p = 0.0516$; G x A interaction: $F(1, 36) = 0.01645$, ns). (**D**) Cued fear memory recall: 24h after the contextual memory recall, when re-exposed to the aversive tone, *Dcx* KO mice froze significantly less than WT and cued memory decreased significantly with age, (ANOVA: Genotype, $F(1, 36) = 14.98$, $p = 0.0004$; Age: $F(1, 36) = 13.16$, $p = 0.0009$; G x A interaction: $F(1, 36) = 1.251$, ns). Values represent means +/- SEM. * vs WT and \$ vs Young, * < 0.05, ** < 0.01, **** < 0.0001.

Supplementary information

Supplementary Fig 1. WT and *Dcx* KO hippocampal neuron morphology *in vitro*.

At DIV3, the *Dcx* mutation affected neither the branching complexity (**A**, ANOVA: Genotype, $F(1, 1036) = 0.3535$, ns; Process: $F(3, 1036) = 196.2$, $P < 0.0001$; G x P interaction: $F(3, 1036) = 0.2558$, ns), nor the total length of processes (**B**, ANOVA: Genotype, $F(1, 350) = 0.3464$, ns; Process: $F(1, 350) = 207.6$, $p < 0.0001$; G x P interaction: $F(1, 350) = 0.05139$, ns), that only depends on the process: the main process is defined as the longest neurite, and somal processes are all other neurites originating from the soma. Primary processes originate from the main or somal processes, secondary processes from primary ($n = 118-132$ neurons from 9-10 embryos from 5 cultures per genotype). Values represent means \pm SEM.

Supplementary Fig 2: Golgi apparatus size and shape in CA3 neurons *in vitro* and *in vivo*.

(A) WT (left) and KO (right) primary hippocampal neurons at DIV3 labeled with Tuj1 (microtubules, red), GM130 (GA, green), and Hoechst. Scale bar = 10 μ M. **(B)** GA volume at DIV3 was not significantly different between genotypes (Unpaired *t*-test, $t(13) = 1.369$, $n = 66-75$ neurons per genotype from 7 WT and 6 KO embryos from 3 litters/cultures). **(C)** At DIV9, the number of GA compartments per neuron and **(D)** the length of GA protrusion into a single process was not significantly different between WT and *Dcx* KO (Mann-Whitney test, $n = 105-114$ neurons per genotype from 5-6 embryos from 3 cultures). *In vivo*, in P7-8 CA3 pyramidal neurons, the number of GA compartments **(E)** and GA volume **(F)** were not significantly different between WT and *Dcx* KO cells (Unpaired *t*-tests; $t(94) = 0.2639$ (E), $t(94) = 0.2343$ (F), $N = 66$ WT, 33 KO neurons). Values represent means \pm SEM or median, min and max values.

Supplementary Fig 3. Quantitative RT-PCR, transcriptome and morphological analyses.

(A) Y-axis corresponds to relative fluorescence units. Up-regulation compared to WT is indicated as values greater than 1 and down-regulation as values lower than 1. Results are presented as the ratio of means ($n = 3-5$ samples per genotype per layer, $p < 0.05$, Student's *t*-tests for each ratio). **(B,C)** DAVID gene ontology analysis for genes up- and downregulated in *Dcx* KO SPE compared to *Dcx* KO SPI (for transcripts with $p < 0.01$). **(D)** DAVID gene ontology analysis for genes up- and downregulated in *Dcx* KO SPE compared to WT (for transcripts with $p < 0.01$). **(E)** Cell type enrichment, compared to Tasic et al (2016). **(F-H)** Altered distribution of NPY+ cells in the adult *Dcx* KO CA3 region. Increased presence of NPY+ cells (red) within pyramidal (Pyr) cell layers (white filled triangles) rather than in the *stratum radiatum* (Rad) or *stratum oriens* (Ori) (arrows) in the *Dcx* KO CA3 compared to WT; Hoechst staining shown in green. **(G)** Average percent of NPY+ cells within

Rad and Ori were significantly decreased in KO ($p = 0.002$ and $p = 0.003$, respectively; Student t -test) and significantly increased in *Dcx* KO Pyr ($p = 0.001$, Student's t -test; $N = 6$ mice per genotype, 4-8 sections per mouse). **(H)** For *Dcx* KO cells located within either the SPI and SPE Pyr layers, significantly less cells were located in SPE (Student t -test, $p = 0.034$). * vs WT, and \$ vs Young. * < 0.05 *** < 0.001 .

Supplementary Fig 4. Mitochondria and GA N/cell, nucleoli measurements

(A) Quantitative analyses showing that the number of mitochondria per cell differed among CA3 layers, but was not affected by aging (ANOVA: CA3 layers, $F(2, 312) = 4.797$, $p = 0.0089$; age: $F(1, 312) = 9.908$, ns; CA3xage interaction: $F(2, 312) = 2.192$, ns). **(B)** The number of Golgi apparatus fragments per cell was higher in KO compared to WT layers and only increased with aging in WT mice (ANOVA: CA3 layers, $F(2, 293) = 2.946$, ns; age: $F(1, 293) = 0.3848$, ns; CA3xage interaction: $F(2, 293) = 7.736$, $p = 0.0005$). **(C)** Compared to the WT layer, nucleolus diameter was significantly reduced in both SPE and SPI layers, even from young adult stages (ANOVA: CA3 layers, $F(2, 553) = 137.7$, $p < 0.0001$; age: $F(1, 553) = 4.018$; CA3xage interaction: $F(2, 553) = 13.52$, $p < 0.0001$). In addition, whereas nucleolus diameter slightly increased in aging WT animals, it remained stable in the SPE layer and significantly decreased in the SPI layer. This remained almost identical when normalizing nucleolus diameter to nuclear size **(D)**, ANOVA: CA3 layers, $F(2, 341) = 37.74$, $p < 0.0001$; age: $F(1, 341) = 15.70$, $p < 0.0001$; CA3xage interaction: $F(2, 341) = 12.81$, $p < 0.0001$. Values represent means \pm SEM. * vs WT, # vs SPE and \$ vs Young. * < 0.05 , ** < 0.01 , *** < 0.001 , **** < 0.0001 .

Supplementary Fig 5. Body weight and fear conditioning

(A) Comparison of body weight between WT and *Dcx* KO mice in young and mature adults showing no difference between genotypes and similar increase with age (ANOVA: Genotype, $F(1, 67) = 1.483$, ns; Age: $F(1, 67) = 47.51$, $P < 0.0001$; G x A interaction: $F(1, 67) = 0.01278$, ns). **(B)** Quantitative analysis of freezing time during the fear conditioning paradigm, showing no difference in freezing behavior between WT and KO mice, neither during 2 min habituation (Pre-CS/US; ANOVA: Genotype, $F(1, 32) = 0.05584$, ns; Age: $F(1, 32) = 0.0002162$, ns; G x A interaction: $F(1, 32) = 0.1763$, ns), nor during the 2 min post-conditioning (Post-CS/US; ANOVA: Genotype, $F(1, 32) = 0.263$, ns; Age: $F(1, 32) = 0.6648$, ns; G x A interaction: $F(1, 32) = 0.0001619$, ns). \$ vs Young. **** < 0.0001 .

Supplementary Tables

Supplementary Table 1. All data for NA = 0, $p < 0.05$, showing p values and ratios (as previously performed Khalaf-Nazzal et al., 2017). Excel file.

Supplementary Table 2. *Dcx* KO (SPI and SPE) and WT CA3 differentially expressed gene transcript lists showing ratios (> 1.1) and P values ($P < 0.01$) for comparisons between SPI, SPE and WT (SPI vs WT, SPE vs WT, SPI vs SPE). These data were used in Venn diagram and DAVID analyses. Excel file.

Supplementary Table 3. Probes/transcripts commonly up or downregulated in both SPI and SPE vs WT for $P < 0.01$ and ratio > 1.1 are provided. Values are ratios. Gene names and GO term/function are also shown for $p < 0.01$, ratio > 1.2 . Excel file

Supplementary Table 4. qPCR results. Excel file.

Supplementary Table 5. DAVID analyses for gene lists. Excel file.

Supplementary Table 6. Deregulated mitochondrial and Golgi-related genes. Excel file.

Supplementary Table 7. Commonly deregulated P0 and P60 genes. Excel file.

Supplementary Table 8

Electron Microscopy		n	N	m ± SEM	Tukey's post-hoc t tests	Adjusted P Value	Significance
Altered mitochondria (%/cell)	Young WT	57	3	0.685 ± 0.24	Young: WT vs. SPE	< 0.0001	****
	Young SPE	39	3	9.365 ± 1.71	Young: WT vs. SPI	ns	/
	Young SPI	47	3	1.848 ± 0.47	Young: SPE vs. SPI	< 0.0001	****
	Mature WT	57	4	2.043 ± 0.29	Mature: WT vs. SPE	< 0.0001	****
	Mature SPE	61	5	12.793 ± 1.32	Mature: WT vs. SPI	< 0.0001	****
	Mature SPI	57	5	12.069 ± 1.06	Mature: SPE vs. SPI	ns	/
					WT:Young vs. Mature	ns	/
					SPE:Young vs. Mature	ns	/
					SPI:Young vs. Mature	< 0.0001	****
Altered GA (%/cell)	Young WT	54	3	22.68 ± 3.79	Young: WT vs. SPE	< 0.0001	****
	Young SPE	39	3	55.70 ± 5.04	Young: WT vs. SPI	< 0.0001	****
	Young SPI	42	3	54.32 ± 4.98	Young: SPE vs. SPI	ns	/
	Mature WT	56	4	26.95 ± 3.63	Mature: WT vs. SPE	< 0.0001	****
	Mature SPE	65	5	62.38 ± 4.25	Mature: WT vs. SPI	< 0.0001	****
	Mature SPI	53	5	54.61 ± 4.88	Mature: SPE vs. SPI	ns	/
					WT:Young vs. Mature	ns	/
					SPE:Young vs. Mature	ns	/
					SPI:Young vs. Mature	ns	/
Inclusion (n/cell)	Young WT	56	3	1.84 ± 0.44	Young: WT vs. SPE	ns	/
	Young SPE	39	3	2.51 ± 0.24	Young: WT vs. SPI	ns	/
	Young SPI	47	3	1.57 ± 0.2	Young: SPE vs. SPI	ns	/
	Mature WT	46	3	3.17 ± 0.39	Mature: WT vs. SPE	ns	/
	Mature SPE	51	4	4.2 ± 0.36	Mature: WT vs. SPI	ns	/
	Mature SPI	46	4	4.09 ± 0.48	Mature: SPE vs. SPI	ns	/
					WT:Young vs. Mature	0.0323	*

					SPE: Young vs. Mature	0.0081	**
					SPI: Young vs. Mature	< 0.0001	****

Journal Pre-proof

Nucleus diameter (μm)	Young WT	121	12.22 ± 0.21	Young: WT vs. SPE	ns	/
	Young SPE	127	11.72 ± 0.19	Young: WT vs. SPI	0.0003	***
	Young SPI	80	10.97 ± 0.28	Young: SPE vs. SPI	0.0236	*
	Mature WT	138	12.30 ± 0.14	Mature: WT vs. SPE	< 0.0001	****
	Mature SPE	155	11.48 ± 0.13	Mature: WT vs. SPI	< 0.0001	****
	Mature SPI	113	9.61 ± 0.19	Mature: SPE vs. SPI	< 0.0001	****
				WT:Young vs. Mature	ns	/
				SPE:Young vs. Mature	ns	/
			SPI:Young vs. Mature	< 0.0001	****	
Nucleolus diameter (μm)	Young WT	86	2.12 ± 0.08	Young: WT vs. SPE	< 0.0001	****
	Young SPE	99	1.57 ± 0.05	Young: WT vs. SPI	< 0.0001	****
	Young SPI	65	1.46 ± 0.07	Young: SPE vs. SPI	ns	/
	Mature WT	108	2.38 ± 0.06	Mature: WT vs. SPE	< 0.0001	****
	Mature SPE	111	1.49 ± 0.05	Mature: WT vs. SPI	< 0.0001	****
	Mature SPI	90	0.96 ± 0.06	Mature: SPE vs. SPI	< 0.0001	****
				WT:Young vs. Mature	0.0102	*
				SPE:Young vs. Mature	ns	/
			SPI:Young vs. Mature	< 0.0001	****	
GA (n/cell)	Young WT	54	2.3 ± 0.1	Young: WT vs. SPE	0.0005	***
	Young SPE	35	3.51 ± 0.34	Young: WT vs. SPI	0.0032	**
	Young SPI	42	3.33 ± 0.29	Young: SPE vs. SPI	ns	/
	Mature WT	56	3.11 ± 0.19	Mature: WT vs. SPE	ns	/
	Mature SPE	56	2.75 ± 0.16	Mature: WT vs. SPI	ns	/
	Mature SPI	43	2.98 ± 0.21	Mature: SPE vs. SPI	ns	/
				WT:Young vs. Mature	0.0180	*
				SPE:Young vs. Mature	ns	/
			SPI:Young vs. Mature	ns	/	
Mitochondria (n/cell)	Young WT	57	38.7 ± 2.51	Young: WT vs. SPE	ns	/
	Young SPE	39	38.54 ± 3.98	Young: WT vs. SPI	0.0246	*
	Young SPI	47	29.87 ± 1.98	Young: SPE vs. SPI	ns	/
	Mature WT	57	37.10 ± 2.5	Mature: WT vs. SPE	ns	/
	Mature SPE	61	30.23 ± 1.58	Mature: WT vs. SPI	ns	/
	Mature SPI	57	31.56 ± 1.76	Mature: SPE vs. SPI	ns	/

					WT:Young vs. Mature	ns	/
					SPE:Young vs. Mature	ns	/
					SPI:Young vs. Mature	ns	/

* < 0.05 ** < 0.01 *** < 0.001 **** < 0.0001.

Supplementary Table 9

Behavioral tests		N	m +/- SEM	Tukey's post-hoc t tests	Adjusted P Value	Significance
Cyclotron : locomotion	Young WT	13	280.9 ± 19.9	Young: WT vs. KO	0.0127	*
	Young KO	16	205.8 ± 14.7	Mature: WT vs. KO	ns	/
	Mature WT	11	154.2 ± 17.5	WT:Young vs. Mature	< 0.0001	****
	Mature KO	13	132.6 ± 17.2	KO:Young vs. Mature	0.0156	*
Open-field : locomotion	Young WT	12	1459.8 ± 213.5	Young: WT vs. KO	ns	/
	Young KO	14	966.2 ± 124	Mature: WT vs. KO	ns	/
	Mature WT	11	567.1 ± 123.6	WT:Young vs. Mature	0.0054	**
	Mature KO	13	282.9 ± 94.9	KO:Young vs. Mature	0.0273	*
Cued memory	Young WT	8	67.3 ± 5	Young: WT vs. KO	ns	/
	Young KO	8	53.1 ± 3.8	Mature: WT vs. KO	0.0020	**
	Mature WT	11	54.3 ± 5.3	WT:Young vs. Mature	ns	/
	Mature KO	13	28.6 ± 4.9	KO:Young vs. Mature	0,0083	**
Contextual memory	Young WT	8	50.8 ± 4.2	Young: WT vs. KO	ns	/
	Young KO	8	39.9 ± 4.8	Mature: WT vs. KO	0.0437	*
	Mature WT	11	44.5 ± 2.6	WT:Young vs. Mature	ns	/
	Mature KO	13	32.7 ± 2.4	KO:Young vs. Mature	ns	/
Body weight	Young WT	17	23.9 ± 0.6	Young: WT vs. KO	ns	/
	Young	20	24.7 ± 0.6	Mature: WT vs.	ns	/

	KO			KO		
	Mature WT	15	28 ± 0.5	WT: Young vs. Mature	< 0.0001	****
	Mature KO	19	28.6 ± 0.5	KO: Young vs. Mature	< 0.0001	****

* < 0.05 ** < 0.01 *** < 0.001 **** < 0.0001.

Journal Pre-proof

Author contributions

MS: Investigation, Methodology, Analysis, Conceptualization; MNB: Investigation, Methodology, Analysis, Conceptualization, Writing, Supervision; RKN: Investigation, Methodology, Analysis; GA: Investigation, Methodology; GG: Methodology; EB: Investigation, Methodology; CCD: Investigation, Methodology, Analysis, Writing; VL: Methodology; RO: Investigation, Methodology, Analysis, Conceptualization, Supervision; JFD: Resources, Supervision; FF: Conceptualization, Funding acquisition, Analysis, Data Curation, Resources, Supervision, Validation, Writing, Review and Editing.

Journal Pre-proof

Highlights

- Neurodevelopmental *Dcx* mutation leads to persistent hippocampal abnormalities
- Adult mutant neurons exhibit Golgi apparatus and mitochondria alterations
- In mutant mice, behavioral defects appear earlier and are more severe with aging

Journal Pre-proof